Research Square

Preprints are preliminary reports that have not undergone peer review.
They should not be considered conclusive, used to inform clinical practice,
or referenced by the media as validated information.

Biomimic opto-nanobiointerface enables multiscale biomodulation

Menglin Chen

menglin@bce.au.dk

Aarhus University https://orcid.org/0000-0002-2721-651X

Christoph Müller

Aarhus University

Yuge Zhang

Aarhus University

Lingyuan Meng

University of Chicago https://orcid.org/0000-0003-1690-586X

Anna Kalatanova

University of East Finland

Jesper Guldsmed Madsen

Aarhus University

Kjeld Kaj Klompmaker

Aarhus University

Thomas Stax Jakobsen

Aarhus University https://orcid.org/0000-0002-5393-3918

Asbjoern Cortnum Joergensen

Aarhus University

Anne Louise Askou

Aarhus University

Ge Huang

University of Copenhagen

Wen Li

University of Chicago

Rasmus Schmidt Davidsen

Aarhus University https://orcid.org/0000-0002-5782-9018

Toke Bek

Aarhus University

Nikos Hatzakis

University of Copenhagen https://orcid.org/0000-0003-4202-0328

Thomas Corydon

Aarhus University https://orcid.org/0000-0003-3588-6350

Henri O Leinonen

University of East Finland

Bozhi Tian

University of Chicago https://orcid.org/0000-0003-0593-0023

Mingdong Dong

Aarhus University https://orcid.org/0000-0002-2025-2171

Article

Keywords:

Posted Date: December 24th, 2024

DOI: https://doi.org/10.21203/rs.3.rs-5333854/v1

License: This work is licensed under a Creative Commons Attribution 4.0 International License.
Read Full License

Additional Declarations: There is **NO** Competing Interest.

Abstract

Virtually all organic material on Earth has been produced converting solar energy through photosynthesis in chloroplasts, a sack-like, double membrane organelle in plants and algae, where transmembrane electron transfer occurs from lumen to stroma. Although animals hardly harness the power of photosynthesis, their bioelectrical signals extensively regulate complex electrophysiological behaviors, rendering it a superior target for biomedical innovation. Here a crude structural mimicry of chloroplast has led us to discover that hollow sphere graphitic carbon nitride nanoparticles (hg-C_3N_4 NPs) endowed non-genetic, subcellular and intercellular photo-modulation of various excitable and non-excitable cells, accumulatively achieving modulation at tissue/organ function level. The homogeneous hg-C_3N_4 NPs showed photo-responsiveness via photoelectrochemical and photothermal mechanisms under photocurrent measurement. The hg-C_3N_4 NPs can be spontaneously internalized with excellent cytocompatibility. Using a focusing laser, the hg-C_3N_4 NPs enable intracellular optical stimulation with subcellular resolution, inducing calcium transient release in multiple cells and propagation in primary cardiomyocytes and cardiac fibroblasts. At multicellular scale, optical pacing and synchronization of cardiomyocyte beating is achieved facilely by LED. Further, we demonstrate that hg-C_3N_4 NPs can be safely injected into mouse eyes, restoring light sensitivity in blind mice. Finally, application of hg-C_3N_4 NPs to porcine retinal tissue *ex vivo* confirmed their modulation capability to reactivate RGCs activity under LED photostimulation. Taken together, these nanostructured biomimic semiconductor NPs offer high resolution, leadless optical probing, non-invasive delivery and great biocompatibility, serving as a versatile tool for addressing a range of complex biomedical challenges through subcellular, intercellular and tissue-level photo-modulation across a broad spectrum of scales.

Introduction

The possibility to electrically sense and stimulate living tissue opens unprecedented potential for therapeutic applications [1,2]. Particularly, neural and cardiac disease treatment can benefit from materials allowing electrical modulation of their bioelectric activity [3,4]. As almost all cells are electroactive and respond to electrical signals, electrical stimulation on specific cells needs to be delivered in a precise and controllable manner with high spatiotemporal control [5].

Light is characterized by its excellent spatial and temporal stimulation resolution. Optogenetics through genetically introducing photosensitive channel protein, such as Channelrhodopsin-2 found in green algae, has proven to be a versatile tool to control transmembrane and intracellular bioelectric activity by light trigger, with high cell-specific selectivity and spatiotemporality [6]. However, it requires genetic modifications and concerns immunogenicity of the introduced exogenous transmembrane proteins of often non-mammalian origin [7].

Interfaces between biological systems and nanomaterials open an array of possibilities for non-genetic modulation of bioelectric activity with similar spatiotemporal control [8,9]. Semiconductor materials with

intriguing photoelectric properties, which can be designed in various shapes and patterns at the nanoscale, are promising candidates to achieve the optically active biointerface [10,11]. This is especially true for intracellular electrical interfaces, as the natural scale of organelles ranges within tens and several hundred nanometers [12].

Nanoparticles (NPs) have shown to be able to build tight interfaces with both intra and extracellular membranes [13,14]. Importantly, light as external power source can trigger electrochemical or photothermal effects at the semiconductor particle/cellular interface acting as a leadless electrophysiological modulator [15,16]. An organic semiconductor graphitic carbon nitride (g-C_3N_4) has drawn attention in various fields including battery research [17], hydrogen evolution [18], as well as biomedical applications in biosensors and cancer treatment [19]. Previously, we have first demonstrated that heterojunction of bulk g-C_3N_4 andreduced graphene oxide can control neurite outgrowth under visible-light stimulation [20–22]. The ability of g-C_3N_4 to be fabricated as hollow nanospheres with further improved photoelectronic properties broadens its potential towards 0D optical nanobiointerfaces [23]. Furthermore, injectability makes NPs a versatile tool for electrophysiological modulation for a broad range of tissues, particularly for retinal tissue [14].

Virtually all organic material on Earth has been produced converting solar energy through photosynthesis in chloroplasts, a sack-like, double membrane organelle in plants and algae, where transmembrane electron transfer occurs from lumen to stroma.[24] Herein, a crude mimicry of chloroplast structure has led us to discover that hollow sphere (h)g-C_3N_4 NPs endow electrophysiological modulation of various excitable and non-excitable cells intracellularly and extracellularly, and accumulatively achieve modulation at tissue/organ function level (Fig. 1). Photocurrent measurements revealed the nature of the photoelectrical response of hg-C_3N_4 NPs to be both photoelectrochemical and photothermal, where reactive oxygen species (ROS) quantification further confirmed generation of anodic faradic photocurrents with amplitudes of 30 pA. The hg-C_3N_4 NP can be safely internalized with excellent cytocompatibility. The potential of hg-C_3N_4 as a tool for intracellular light stimulation with subcellular resolution is demonstrated to induce calcium flux in various excitable and non-excitable cells, allowing cell-cell calcium propagation in primary cardiomyocytes and cardiac fibroblasts. Further, the capacity of hg-C_3N_4 NPs for potential cardiac pacing applications was facilely achieved by low intensity LED light. At tissue/organ level, the hg-C_3N_4 NPs endowed neuromodulation of retinal tissue to reactivate retinal ganglion cell activity after intravitreal injection in blind rd10 mice of autosomal recessive retinitis pigmentosa.. This is the first time that biomimic organic semiconductor NPs achieve subcellular, intercellular and tissue-level photo-modulation across a broad spectrum of scales.

Results

Morphological, photoelectrical and chemical characterizations of the hg-C_3N_4 NPs

To achieve hollow spherically shaped hg-C_3N_4 NPs, a tailored silica template with subsequent hydrofluoric acid (HF) etching was employed to achieve submicron shape and size requirements inspired by intracellular organelles and vesicles, especially the remarkable photosynthesis organelle, chloroplast. Scanning electron microscopy (SEM) and transmission electron microscopy (TEM) clearly show the hollow sphere structure of the particles with an inner diameter of around 110 nm and an outer diameter of 190 nm, leaving a controlled amorphous shell of around 80 nm (Fig. 2a, b).

The great light harvesting properties of hg-C_3N_4 NPs could be confirmed by UV-Vis spectroscopy, where hg-C_3N_4 NPs showed up to 4 times higher light absorbance within a range of 350–600 nm, indicating considerably more absorbance in the visible spectrum compared to bulk g-C_3N_4 (Fig. 2g). This effect could be attributed to multiple reflection sites residing in the hollow structure, prolonging the light path length for absorption within the spheres [23]. The atomic force microscopy (AFM) topography image (Fig. 2c) revealed a few single hg-C_3N_4 NPs with a height around 200 nm (Fig. 2d) together with some aggregates, which is similar to the TEM results. Via particle analysis (Fig. 2e), the statistic height of the stacked layer is (383 ± 79) nm, indicating the possible bilayer-stacking. The further particle tracking analysis revealed a mean stokes diameter of (636 ± 209) nm with a corresponding diffusion coefficient of (1.01 ± 0.36) $\mu m^2/s$ (Fig. 2f, and Supplementary Fig. S1), showcasing the possible aggregation of the NPs.

The leadless bioelectric stimulation with photo-responsive particles is based on the production of photoelectrochemical or photothermal effects, both affecting adjacent cell membranes [15,25]. To investigate the nature and magnitude of the photo-response of hg-C_3N_4 NPs, a patch-clamp electrophysiology apparatus with integrated photocurrent measurement set-up was employed (Fig. 3c). The relationship of photocurrent trace amplitude and applied holding currents I_0 provides insight to the nature of the generated photocurrents. As photothermal effects go along with temperature increase, the increased ion mobility leads to reduced pipette resistance and subsequently increased current, directly proportional to the amperage of I_0. On the other hand, photoelectrochemical processes, like capacitive and faradaic currents, are independent from the applied holding current [26]. Figure 3a, together with the non-zero intercept of Fig. 3b, show that both photoelectrochemical and photothermal effects are generated. The sustained current with negative polarity over the entire pulse length and low amplitude around 30 pA for I_0 = 0 nA, is evident of an anodic faradaic current, as opposed to capacitive currents, characterized by the fast charge and discharge processes.

Since faradic photocurrents go along with redox reactions at the semiconductor/electrolyte interface, the generation of ROS is probable. The quantification of H_2O_2, a typical ROS, (Fig. 3d) revealed that indeed 10 µmol/mg of H_2O_2 is produced upon visible light exposure, confirming an electrochemical

process. Together with the photocurrent traces, the hg-C_3N_4 NPs mediated photostimulation is based on both mechanisms, anodic faradaic currents and evident photothermal effects. Both stimulation mechanisms have shown to be able to elicit action potentials in neurons and have been used to modulate cardiac tissue [9,27–30].

Particle internalization and cytocompatibility

Fibroblasts play a vital role in all tissues by contributing to structural integrity [31], and cardiac fibroblasts are specifically coupled in cardiac electrophysiology [32]. Here, NIH/3T3 mouse embryonic fibroblasts were chosen to study the internalization process of hg-C_3N_4 NPs, as efficient internalization is highly important to achieve subcellular resolution. To characterize the spontaneous internalization of hg-C_3N_4 NPs, the inherent blue fluorescence property of hg-C_3N_4 is used to track the particles over time while single cells were continuously imaged. Lysosomes (Lys) are intracellular organelles responsible for uptake, transport, and processing of cargo and can be stained with fluorescent markers. The progressive increase in colocalization of stained Lys with hg-C_3N_4 after 4 h is a strong indicator of successful internalization (Fig. 4a, c and Fig. S2). Fluorescent imaging of live cells further confirms that the hg-C_3N_4 NPs were indeed localized within the intracellular space (Fig. 4b).

Moreover, Fig. 4e and supplementary video S1 shows internalization of several hg-C_3N_4 NPs over a period of 12 h. Tracking of the particles demonstrates a clear directionality of the particles from the extracellular space towards the center of the cell, close to the nucleus (Fig. 4f). The directedness is used as a quantitative indicator for the loss of random mobility of internalized particles compared to non-internalized particles (Fig. 4g). The angle Θ of the directionality vector of the particle relative to the direction of the nucleus is used as a measure for directionality. Here, the median cos(Θ) for internalized particles is 0.91, indicating movement angle Θ ± 25° in the direction of the nucleus. Non-internalized particles show random mobility with cos(Θ) distributed broadly between 1 (directed movement, Θ =0°), 0 (perpendicular movement, Θ =90°), and − 1 (movement in opposite direction, Θ = -180°) [33]. This decrease in random mobility is thus a strong indicator of successful internalization.

To investigate hg-C_3N_4 NPs toxicity and influence on cell growth, a lactate dehydrogenase (LDH) assay, live/dead staining, and cell counting kit 8 (CCK-8) proliferation assay was conducted. The LDH assay could not show any considerable toxic effects of hg-C_3N_4 NPs particles against NIH/3T3 cells (Fig. 4d). Live dead staining could not show difference in cell death or viability of NIH/3T3 treated with gh-C_3N_4 and non-treated cell (Supplementary Fig. S3a). Further, the CCK8 assay shows that hg-C_3N_4 NPs do not influence the proliferation rate of NIH/3T3 cells, confirming the cytocompatibility of hg-C_3N_4 NPs (Supplementary Fig. S3b).

As photostimulation of hg-C_3N_4 NPs could cause potential phototoxicity we tested the effect of high dose 450 nm blue LED light (75 mW/cm^2, 1 Hz, 100 ms pulse width) for 10 minutes bidaily. Live dead

staining did not show effects caused by the light treatment, compared to non-light treated groups (Supplementary Fig. S3). Light treatment did lead to a decreased proliferation rate, however, when cells were treated with both hg-C_3N_4 NPs and light, the proliferation rate was normalized after 8 days. It has been reported that high doses of blue light can negatively influence cells [34], and therefore the LED light intensities used in this study were limited to 10–30 mW/cm^2.

The factors that influence the mechanism of internalization are manifold, with particle size and shape being among the most important particle properties [35,36]. The clear directedness quantified as cos Θ (Fig. 4g), as well as the clustering of particles around the nucleus (Fig. 4e) could be indicative of a phagocytosis or endocytosis driven mechanism (Fig. 4h) [37,38]. After encountering the cell membrane, the particles could get engulfed in a phagosome. The directed transport towards the perinuclear region of cells could be enabled by active transport with the cytoskeleton proteins, where particles form clusters and aggregate [39].

Biological modulation at subcellular and cellular level

Subcellular photostimulation of non-excitable cells

The ability of the particles to induce light-triggered intracellular bioelectric activity with subcellular resolution was investigated by monitoring calcium flux under focused laser beam stimulation of single internalized particles. hg-C_3N_4 NPs showed strong fluorescence in the green channel, enabling simplified identification of internalized hg-C_3N_4 NPs. A focused 473 nm (8.8 mW/μm^2) laser beam with a pulse width of 200 ms and spot size of 3 μm was employed to stimulate the particles. The laser pulse alone could not provoke any change in calcium dynamics in NIH/3T3 fibroblast cells (Supplementary video S2). When particles were present, photostimulation led to an immediate calcium flux through the cytosol originating from the stimulated particle location (Fig. 5a, Supplementary video S3–4), as evidenced by the vector direction graphic (Fig. 5a). For 3T3 cells, the average calcium flux velocity was (2.4 ± 3.8) μm/s.

The versatility of hg-C_3N_4 NPs to study intracellular bioelectric activity of non-excitable cells was also demonstrated by HELA cells (Fig. 5b). A single 200 ms laser pulse led to an immediate intracellular calcium flux with a prolonged increase in intracellular calcium, evident by the sustained increase in fluorescence intensity (Supplementary video S5–6). The average velocity of the calcium flux in HELA cells was determined to be (1.3 ± 2.7) μm/s.

Photostimulation of excitable cells and intracellular signal propagation

The application of hg-C_3N_4 NPs to study intracellular bioelectric activity of excitable cells was then demonstrated by cardiomyocytes (CM), which play a key role in heart tissue muscle contraction. We tested the ability of hg-C_3N_4 NPs to electrically modulate primary rat CMs and primary rat cardiac fibroblasts (CFs). hg-C_3N_4 NPs associated with CMs were directly stimulated, resulting in immediate intracellular calcium flux and beating (Fig. 5e, Supplementary video S7). Intriguingly, the calcium flux of the stimulated cell led to calcium flux and beating of three adjacent coupled CMs. The mechanism of this signal propagation is typical for coupled CMs and relies on interconnected connexin gap junctions, enabling synchronous beating essential for the physiological function of the heart [32].

Cell-cell signal propagation was observed not only between the CMs, but also CFs. CFs express a plethora of ion channels, mainly potassium (K^+) channels and mechanosensitive channels, that contribute to their resting membrane potential [40–43]. Indeed, a stimulated primary CF propagated the calcium transient to an adjacent CF with a velocity of (8.8 ± 16.2) µm/s (Fig. 5c, Supplementary video S8). Direct coupling of cardiomyocytes and fibroblasts via connexin-based gap junctions is supported by compelling evidence [32,44,45]. Stimulating of a primary CF adjacent to CM led to a similar observation, when the intracellular calcium flux of the fibroblast reached the outer cell membrane with (4.4 ± 8.5) µm/s, the adjacent CM started with continues beating (Fig. 5d, Supplementary video S9).

Interval training of cardiomyocytes

The injectability of NPs makes them an attractive non-invasive alternative to conventional electronic pacemaker therapy. As the stimulation of single cardiomyocytes via laser has proven feasible, we next wanted to apply interval training to many cardiomyocytes simultaneously to synchronize beating and align to common beating frequency using low intensity (10 mW/cm^2, λ = 450 nm) LED as light source. When HL-1 cardiomyocytes were cultured together with hg-C_3N_4 NPs and LED photostimulation with a frequency of 1 Hz and 100 ms pulse width was applied for 10 min, the beating frequency changed from an irregular non-synchronized pattern between 0.5 and 2 Hz to a more synchronized pattern of 2 Hz (Fig. 6a, b). This effect was even more pronounced after 30 min of stimulation. Further, the calcium flux appeared to travel as a directional synchronized wave through the cardiomyocyte cell sheet, when both hg-C_3N_4 NPs and photostimulation were applied (Fig. 6c, Supplementary video S10-12). Cardiomyocytes cultured without hg-C_3N_4 NPs remained in a state of unsynchronized beating behavior. Light stimulation alone led to an increase in beating frequency around 1.5 Hz, however, without the desired synchronization and directionality of the calcium wave (Supplementary Fig. S4).

Interestingly cardiomyocyte beating was not synchronized to the stimulation frequency of 1 Hz, but to 2 Hz. This might be attributed to the fact the natural heart beating of mice is much higher than 1 Hz, and to our knowledge no decrease of beating frequency could be achieved in pacing experiments [27,29,46]. This could mean that cardiomyocytes were trained at 1 Hz at their every second beat to achieve a final beating rate of 2 Hz.

Therapeutic biomodulation in the retina

The eye is a remarkable organ, and retinal tissue is an essential part of this system playing a critical role in converting energy from photons of visible wavelengths to electrical signals, preprocessing the visual signals, and then mediating the signals to the brain for further processing and interpretation. This complex retinal process relies on the interplay of different types of neurons within the tissue. Among these, retinal ganglion cells (RGCs) are responsible for receiving input from the sensory photoreceptors, through retinal interneurons (bipolar cells), and then transmitting this information to the visual areas of the brain. Bioelectronics have emerged as a promising approach for restoring vision, especially if the device is responsive to light [47]. Here, we further explore the potential of hg-C_3N_4 NPs as an injectable retinal prosthesis using living mice as well as porcine retina *ex vivo*.

To test the feasibility of safe hg-C_3N_4 NP delivery to the target, biodistribution and retinal integrity were assessed after intravitreal delivery to wild-type (WT) C57BL/6JRj mice (Fig. 7a). The intravitreal injection of hg-C_3N_4 NPs into mouse eyes resulted in the visible settlement of particle aggregates on the retinal surface immediately adjacent to the RGCs and their axons as observed in fundus images and optical coherence tomography scans 14 days post-injection (Fig. 7b). Additionally, the hg-C_3N_4 NPs aggregates could be clearly identified on top of the RGCs using fluorescent imaging of retinal cross sections (Fig. 7d-e). The integrity and thickness of retinal layers were preserved (Fig. 7b, c) with no significant differences in total retinal thickness ($p = 0.57$) or the thickness of individual layers between baseline and day 14 post-injection. Thus, intravitreal injection seems to be a safe delivery route for hg-C_3N_4 NPs.

Next, to assess the potential of the intervention to restore light sensitivity in visually impaired mice (Fig. 7f), we administered the NPs into *Pde6β*^{rd10} mice intravitreally. These mice (in short rd10 mice) represent a translationally relevant mouse model of autosomal recessive retinitis pigmentosa and they lose light sensitivity by ~ 8 weeks of age, as measured by corneal electroretinogram (ERG) recordings[48]. We injected the hg-C_3N_4 NPs ($n = 7$), and control particles; SiO_2 ($n = 3$) and Red F ($n = 4$), into both eyes of rd10 mice at 12 weeks of age. The delivery of NPs was confirmed with fundoscopy immediately after the injections. Age-matched C57BL/6J WT mice served as healthy controls. One month after injections, scotopic ERGs were recorded under ketamine and medetomidine (KM) anesthesia to test if the 16-week-old rd10 had retained or recovered any photoreceptor function. The absence of ERG signals in any of the rd10 mice confirmed the lack of light sensitivity from the photoreceptors (Fig. 7g). Of note, the flash ERG response arises from photoreceptor hyperpolarization (a-wave) and subsequent bipolar cell depolarization (b-wave), but the electrical activity in the level of RGCs is not detected because similar amount of ON and OFF pathways is activated leading to signal cancellation[49]. Therefore, other tests than the ERG are required for testing RGC light sensitivity and downstream visual function.

To assess function with a test that requires activation of visual areas of the brain, we allowed the mice to recover for four weeks and then performed a behavioral light-dark box (LDB) test at 20 weeks of age. In this test, the animals are allowed to freely roam in a test environment with two otherwise matching

compartments except that one compartment is brightly illuminated, and the other one is dark. These two compartments are connected to each other by a small passage. In theory, if the animals are blind to ambient light they will spend equal time exploring both compartments, whereas seeing mice typically have preference to darkened environment due to natural fear of open and lit spaces[50]. The LDB test indicated that some WT and hg-C_3N_4 NP-injected rd10 mice had relatively strong preference to stay in the darkened compartment, although ANOVA analysis comparing group means did not show any statistically significant effect (Fig. 7h; $F_{3,16} = 2.30$, $p = 0.16$). To evaluate light responses in the visual cortex more precisely, we turned to recordings of visual evoked potentials (VEPs) using skull screw electrodes inserted over the primary visual cortices under urethane anesthesia (Fig. 7f). As expected, due to lack of ERGs, the SiO_2- or Red F-particle-injected rd10 mice did not show any VEPs (Fig. 7i). Instead, two out of seven hg-C_3N_4-injected rd10 mice did show a small VEP and one mouse responded relatively strongly to light flashes at intensities of 5, 50 and 500 cd·s/m^2, albeit with substantially slower response kinetics compared to healthy WT mice (Fig. 7i-k). With respect to rd10 mice, the results from the LDB and VEP assays corresponded, as the VEP-responding mice also showed dark preference in the LDB test (max VEP: 23, 15 and 65 μV; dark preference: 63, 70 and 78%, respectively). When the rd10 mice were allocated to non-responding and responding groups and the LDB test results were re-analyzed, it became apparent that three subjects recovered meaningful light sensitivity after the intravitreal hg-C_3N_4 NP intervention.

Our inability to successfully treat the majority of rd10 mouse eyes with hg-C_3N_4 NPs prompted us to further test retinal light sensitivity in an *ex vivo* paradigm that avoids the well-known delivery challenges of therapeutics into the mouse eye. Here, porcine retinal tissue was placed on a microelectrode array (MEA) with the RGCs facing up (Fig. 8a). To test the viability of the retina, we applied a 1 ms visible light LED pulse (450 nm) and were able to record light evoked potentials with mean peak-peak amplitude of 11.0 μV that are typical of retina response across all channels (Fig. 7b, Supplementary Fig. S5). RGCs produce action potentials in order of several mV, recordable through the photoreceptor layer of around 100 μm thickness [51–53]. We then added hg-C_3N_4 NPs to the tissue and allowed them to settle on the RGC layer (Fig. 7d). With the same light dose (30 mW/cm^2), we observed a drastic increase in mean peak-peak amplitude from 11 to 47.7 μV (Fig. 7b, c, Supplementary Fig. S6). The observed augmentation in peak-peak amplitude can be ascribed to synergy from the activation of photoreceptor cells stimulated solely by the light stimulus and the supplementary sensitization facilitated by hg-C_3N_4 NPs.

To confirm that the recorded signal was indeed of biological nature and consisted of compound action potentials created by the RGCs, we applied Tetrodotoxin (TTX) to prevent the RGCs from producing action potentials. TTX is a highly effective neurotoxin mainly found in different marine organisms, binding to voltage gated sodium channels and inhibiting neuronal firing [54]. When TTX was present the amplitude of the evoked compound action potentials was greatly reduced, confirming that the recorded action potentials are indeed of RGC origin (Fig. 7b, Supplementary Fig. S7). Finally, we conducted a dose response test that showed that even light intensities as low as 8.9 mW/cm^2 can produce light-evoked

potentials when hg-C_3N_4 NPs are present (+ P) (Fig. 8e, f), while peak-peak amplitudes recorded with 3.2 mW/cm^2 + P were not distinguishable from peak-peak amplitudes recorded with 26.1 mW/cm^2 without particles (- P). It is important to note that the light-evoked peak-peak amplitudes in the dose response test appear to be considerably lower compared to the experiment shown in Fig. 8b, c. The reason might not only lie in the lower light intensities, but fluctuations of the physiological state of the porcine retina caused by differences between individual animals/specimens.

Discussion

In summary, we have demonstrated the versatility of chloroplast-mimicking hg-C_3N_4 NPs for multiscale photo-modulating electrophysiology, at the subcellular level, intercellular level, and tissue level. Tools to probe intracellular and intercellular electrophysiological mechanisms are crucial for studying physiological and pathological pathways, not only prevailing in cardiovascular and neurodegenerative diseases. For instance, a recently discovered hub of highly connected glioma cells, similar to heart 'pacemaker' cells, drive calcium propagation through tumor microtube networks and promote expansion of the lethal malignant glioma via activation of MAPK and NF-κB signaling pathways [55]. Nowadays, these studies are often hampered by the available disruptive methods [56]. We present the hg-C_3N_4 as organic semiconductor NPs to leadless modulation of single cell signaling across a broad spectrum of excitable and non-excitable cell types and endow intercellular signal propagation by applying laser stimulation with subcellular resolution. Accumulatively, the capability of hg-C_3N_4 NPs to pace cardiomyocytes network's synchronous beating was achieved by simple LED stimulation. Though being out of the scope of the current work, application of optical-fiber-coupled endoscope[57] should further enable in vivo heart pacing and clinical translation.

The hg-C_3N_4 NPs could be safely internalized, an important feature for stimulation on the intracellular level. Clear directedness in the movement of the internalized particles gives an indication of active transport, possibly due to an endocytosis or phagocytosis driven mechanism (Fig. 4b) [39,58]. Specifically, a clathrin-mediated endocytosis and phagocytosis could be a likely route as one dominant internalization mechanism for NPs [37]. Experiments involving clathrin-blockers such as chlorpromazine can help to gain a deeper understanding of the hg-C_3N_4 internalization mechanism [59].

The photo-response mechanism of hg-C_3N_4 NPs could be revealed to be of anodic faradaic photocurrent and photothermal nature. The mechanism behind the observed intracellular calcium transient might be attributed to hg-C_3N_4 NPs interacting with calcium storing organelles like the endoplasmic reticulum (ER, Fig. 5a), possibly similar to the work of Rotenberg et al. on the inorganic silicon-nanowires [60]. As we could show that the generated faradaic photocurrents go along with ROS production (Fig. 1b, and 3d), ROS might interact with organelles leading to intracellular calcium release [61,62]. Further, the photothermal contributions might act as an additional factor leading to the observed calcium release. It has been shown that photothermal effects can cause membrane poration [63], and may lead to release of

calcium. It is thus plausible that both faradaic electrochemical and photothermal effects act together to achieve intracellular membrane depolarization, as both effects have been found to modulate bioelectrical behavior independently [9,15]. It is important to note that despite the similar stimulation mechanism, the chemical stability of g-C_3N_4 [19] poses a unique advantage compared to silicon nanowires [64], which have been shown to gradually degrade under physiological conditions.

The anodic currents lead to a predominately oxidative reaction, and subsequent generation of H_2O_2 e.g. by the oxidation of H_2O [62]. However, the interfacial reactions are complex and there are other plausible pathways leading to ROS generation [65]. ROS like H_2O_2 are important signaling molecules involved in many fundamental physiological processes [66], even interacting with neuronal ion channels [67,68]. However, the physiological ROS concentration is well controlled around 1–5 µM and high concentration of ROS can be toxic and cause cell damage [66,69]. Convincingly, neither cytotoxic effects nor inflammation induction *in vivo*[70] could be observed in this study.

Photostimulation appears to be a particularly promising approach to achieve high spatiotemporal resolution. Here, the photo-response of hg-C_3N_4 NPs triggered at low intensity (8–30 mW/cm^2) within the visible light range mediated pronounced photo-responses in porcine retinal tissue *ex vivo* in the present study. Considerably, the feasibility of safe and therapeutic *in vivo* delivery to the murine retina suggests hg-C_3N_4 NPs as an injectable retinal prosthesis that could enable vision restoration in patients with severe photoreceptor loss due to e.g. inherited retinal degenerations or age-related macular degeneration. Although the low tissue penetration depth of blue light might limit the use of hg-C_3N_4 NPs for some applications, red-shifting the absorbance of g-C_3N_4 towards near infrared has been proven feasible [71]. Furthermore, as the focused ultrasound has been utilized to generate ROS for vinyl monomer polymerization based volumetric bioprinting,[72] emerging piezoelectric property of g-C_3N_4[73] could further broaden the potential application of hg-C_3N_4 NPs for deep tissue stimulation.

Materials and Methods

Synthesis of silica template

The silica template was synthesized according to the classical Stöber method [23]. In detail, the mixed solution containing 4.0 mL of aqueous ammonia (28 wt%), 74.0 mL of ethanol and 10.0 mL of deionized water were stirred vigorously at 30˚C for 1h. Then, 5.6 mL of tetraethoxysilane (TEOS) was slowly added to the above mixture under continuous stirring and stood still for 1 h to yield uniform monodisperse silica cores. Next, 3.56 mL of TEOS and 1.71 mL of n-octadecyltrimethoxysilane (C_{18}TMOS) were added dropwise to the above solution while stirring. After the solution was dropped, the mixture was continued to stir for 15 min to form a thin silica shell around the dense silica core. Subsequently, the mixed solution was allowed to stand for 3 h to promote the cohydrolysis and condensation of the TEOS and C_{18}TMOS. The mixed solution was centrifuged, washed in DI water and ethanol, dried at 80˚C and calcined at 550˚C

for 6h in air. Finally, the obtained silica template was neutralized with a 1 M HCl solution and dried at 80˚C overnight.

Synthesis of hg-C_3N_4 NPs

A solution of 1.0 g of the silica template and 5.0 mL of cyanamide aqueous solution (50 wt%) was mixed for 30 min in a flask, then the mixture was ultrasonicated in vacuum at 60˚C for 3 h and stirred at 60˚C overnight. After centrifugation and drying, the products were transferred to chemical vapor deposition (CVD) furnace for calcination and heated to 550°C under flowing N_2 for 4 h with a heating rate of 4.4˚C min^{-1}. The obtained products were treated with 4 M NH_4HF_2 for 12 h to remove the silica template. In the last, the yellow powders were centrifuged, washed three times in DI water and once in ethanol, and then dried in vacuum at 60˚C for 10 h to obtain the final HCNS products.

Electron microscopy

The particles morphology was analyzed by SEM (TM3030Plus, Tabletop microscope, HITACHI). Transmission electron microscopy (TEM, Tecnai G2 Spirit) was used to visualize the hollow-sphere structure. TEM copper grids (Merck) were employed for analysis with an acceleration voltage of 120 kV.

AFM characterization

AFM measurements were performed on commercial Dimension Icon (Bruker, Santa Barbara, USA) using AC160TS-R3 (k = 26 N/m) probe. The topography of hg-C_3N_4 sphere was captured by tapping mode in ambient air. The data processing was completed in Nanoscope Analysis software. The particle analysis was performed in SPIP software.

Cell culture and material seeding

NIH/3T3 and HELA cells were cultured in Dulbecco's Modified Eagle Medium (DMEM) supplemented with 10% fetal bovine serum (FBS), 1% P/S, and 4 mM L-glutamine. All cells were kept at 37˚C and 5% CO_2 and media were changed every second day.

Cardiac cell culture. Primary cardiomyocytes (CMs) and cardiac fibroblasts (CFs) were isolated and harvested from P0-5 neonatal rats following literature [60] and reagents were obtained from Pierce™ primary cardiomyocyte isolation kit (Thermo Fisher Scientific [74]. Basically, the heart tissues were excised into ice cold Hanks' Balanced Salt solution (HBSS) medium without Ca^{2+} or Mg^{2+} and digested with reconstituted papain and thermolysin enzymes. Isolated CFs/CMs hybrid cells were washed with HBSS, seeded onto fibronectin (Sigma)-coated glass bottom imaging dishes, and cultured in high glucose DMEM plus 10% FBS, 1% penicillin–streptomycin, and 1% GlutaMAX. Animal procedures were approved by the University of Chicago Institutional Animal Care and Use Committee (IACUC) and conducted in complete compliance with the IACUC Animal Care and Use Protocol.

Particle co-culture. Before seeding, hg-C_3N_4 NPs were sonicated in ethanol (or treated with UV lights for 15 min) to sterilize and washed and resuspended in phosphate buffered saline (PBS). Harvested

CFs/CMs hybrid cells were enriched in 24-well plates and proliferated until ~ 70% confluency and around 2.0 μg/cm^2 hg-C_3N_4 NPs were seeded into each well.

LDH cytotoxicity assay

The cytotoxicity assay was conducted following the manufacturer's instructions (LDH cytotoxicity kit, Roche). Briefly, 2500 3T3 cells were evenly seeded into sextuplicate wells of a 96-well plate with 100 μL of complete medium. Two groups were examined: one with particles and one without. For the wells with particles, 2.0 μg/cm^2 of hg-C_3N_4 NPs were added.

After 24 hours of incubation, 80 μL of the cell culture medium was collected and centrifuged at 1700 rpm for 5 minutes at 4˚C. The activity levels of lactate dehydrogenase (LDH) were then measured by transferring 50 μL of the supernatant to a new 96-well plate and adding reaction mix containing catalyst and dye in a 1:1 ratio. Subsequently, the plate was incubated in the dark at room temperature for 30 minutes, followed by analysis of absorbance on a Victor Multilabel Reader (PerkinElmer, US) at 490 nm. To establish the toxicity levels, the LDH activity of cells cultured without particles was regarded as the low toxicity control, while that of cells treated with 1% Triton X-100 was marked as high-toxicity control. The relative toxicity levels were calculated using the below equation:

$$\%Cytotoxcitiy = \frac{exp.\ value - low\ control}{high\ control - low\ control}$$

CCK-8 proliferation assay

The effect of particles on cell proliferation was assessed using a Cell Counting Kit-8 (CCK-8, Dojindo). 5000 NIH/3T3 cells were seeded in 96-well plates in sextuplicate. 2.0 μg/cm^2 of h-g-C3N4 particles were added. The CCK-8 assay was performed on days 1, 3, and 8 following the manufacturer’s protocol. Briefly, the culture medium in each well was replaced with CCK-8 solution diluted 1:20 in medium. The cells were then incubated for 2 hours, after which the medium was transferred to a new 96-well plate and fresh culture medium was replenished. Subsequently, the absorbance at 450 nm was analyzed on Victor Multilabel Reader (PerkinElmer, US). The proliferation index is calculated as:

$$Profiferation\ Index = \frac{Ab_x}{Ab_1}$$

with Ab being the absorbance value of the CCK-8 assay measured on day x (x = 1, 3, 8).

hg-C_3N_4 NP internalization

For colocalization and single particle tracking (SPT) an inverted spinning disk confocal microscope (SDCM (Olympus SpinSR10, Olympus, Tokyo, Japan) was applied. The SDCM used an oil immersion 60x objective (Olympus) for recording images and videos with a total pixel width of 183 nm and numerical aperture of 1.4, and a CMOS camera (photometrics PRIME 95B). For colocalization experiments, dual-

imaging was utilized for simultaneously imaging with two laser channels. Excitation wavelengths of 640 nm and 488 nm were used to excite the LysoTracker Deep Red (Invitrogen, L12492) and hg-C_3N_4 NPs.

10.000 NIH/3T3 cells per well were added with the appropriate amount of growth media and are left for incubation at 37˚C, 5% CO_2 for 2 days. On the day of microscopy, each well with cells was washed 3 times with 10 mM HEPES in HBSS buffer prior to addition of 200 µL test solution of hg-C_3N_4 NP dispersion with 0.6 µg/cm^2 and lysosome labelling with LysoTracker Deep Red (diluted 1:20.000). The test solution was incubated for 3 h at 37˚C and 5% CO2. The test solution was then removed and replaced with pre-heated 200 µL 0.6 µg/cm^2 hg-C_3N_4 NPs. For SPT, the Trackpy [75] package in python based on the Crocker-Grier algorithm [76] with in house modification from the Hatzakis lab was used.

For investigating the directedness, a 0.5 mg/mL hg-C_3N_4 NP stock was prepared in PBS by sonication for 15 min. The stock dispersion was diluted in media and added to the cells to achieve a final particle concentration of 0.6 µg/cm^2. The internalization videos were recorded using the Nikon TI2-E inverted microscope and NIH/3T3 cells. Particle tracking of internalized particles was done using Manual Tracking plugin in ImageJ.

Calcium imaging and laser stimulation

To visualize intracellular calcium Cal-520, AM (ab171868, abcam) at 4 µM was used. After incubating the cells with dye in glass bottom dishes at 37˚C for 30 min, the cells were rinsed and incubated for another 30 min at 37˚C in medium. The cells were observed with a 60x oil immersion objective using a Nikon TI2-E inverted microscope. Laser (473 nm) power was calibrated using the PM100D optical power meter (ThorLabs) and S120C photodiode power sensor (ThorLabs).

Isochronal and vector maps were generated using the ImageJ plugin Spiky [77]. An online available macro was used to generate $\Delta F/F_0$ movies [78]. Calcium flux videos were quantified with ImageJ by defining regions of interest around cells and measuring mean gray values (F). As background value (F_0) the mean gray value of an ROI without cells was defined. The mean fluorescence intensity normalized to the background was then calculated as $\Delta F/F_0$ for each individual frame.

HL-1 pacing

HL-1 cells were cultured in 24-well plates at a seeding density of 100,000 cells per well. Upon reaching 90% confluency, particles were added at concentrations of 2.0 µg/cm^2 followed by a 6-hour settling period before initiating calcium imaging.

For calcium flux imaging, cells were stained with Fluo-4 AM (Invitrogen, F14201). Samples were rinsed with Hanks' Buffer (Sigma H6648) supplemented with 0.1 mM norepinephrine (Sigma, A0937), 5 mM glutamax, and 20 mM Hepes (Sigma H0887). Subsequently, cells were incubated with 5 µM Fluo-4 AM diluted in the same buffer for 30 min at 37˚C, 5% CO_2. After rinsing twice, the cells were incubated in the

buffer for an additional 20 minutes. Following the aspiration of the buffer, supplemented Claycomb Medium was added and used during imaging.

Stimulation was performed using light irradiation at a power of 10 mW/cm^2, frequency of 1 Hz, and pulse width of 100 ms. Calcium flux was monitored and recorded via a 10x objective on the EVOS microscope (EVOS m7000) equipped with an onstage incubator (37˚C, 5% CO_2).

Live cell staining

Live cell staining of 3T3 cells was conducted using CellBrite Steady Dye 550 diluted 1:1000 (Biotium) for membrane staining, and Calcein AM (ab141420, abcam) as viability stain. Imaging and Z-stacks were generated using the Nikon TI2-E inverted microscope. Cell viability upon exposure to particles and light was assessed using Live/Dead staining using NIH/3T3 cells cultured for 24 h. The particles (2.0 µg/cm^2) were introduced 6 hours prior to the light stimulation. The staining solution, a combination of 1:1000 Calcein-AM (green dye) and 1:500 Ethidiom iodide (red dye) medium, was added after aspiration of the culture medium and a single rinse with serum-free medium. After adding the staining solution, cells were then incubated for 30 min at 37˚C. Afterwards, the staining solution was discarded, wells were rinsed with PBS, and cells could be examined using a fluorescent microscope (Invitrogen EVOS M7000).

Particle tracking

The ONI Nanoimager was employed for single particle tracking in cell free media to investigate stokes diameter and diffusion coefficient. The maximal frame gab was set to 5, maximal distance between frames was 0.7 µm and the minimum number of steps was set to 20. For particle tracking of internalized particles in 3T3 cells the Manual Tracking plugin for ImageJ was used. Based on the tracking data acquired with Manual Tracking plugin, the directedness was calculated as a parameter for directional movement. The angle Θ was defined as the angle between particle movement direction and direction of the center of an individual cell. The directedness is defined as the cosine of this angle. If particle movement is directed exactly towards the center of the cell the value is 1, whereas the value 0 indicates perpendicular movement, and − 1 movement in the opposite direction. The average directedness was calculated as $\Sigma\cos\Theta_i/n$, where Θ was the angle between the individual movement directionality vector and the directionality vector towards the center of the cell relative to the particle position (n = 8) [33].

UV-vis spectroscopy

UV-Vis spectra were acquired with the GENESYS 150 UV-Visible Spectrophotometer (Thermo Fisher Scientific).

Photocurrent measurement

A detailed protocol on how to acquire photocurrent data has been described previously [26]. Briefly, the setup was based on an electrophysiology patch-clamp aperture. A P-97 micropipette puller was used to pull glass pipettes and achieve a resistance of 2–4 MΩ. A micromanipulator was used to bring a silver

chloride electrode inserted in the glass pipette in close proximity to the particles (< 10 µm). The sample as well as the objective is immersed in PBS. The upright microscope (Olympus, BX61WI) allows to illuminate the sample with a 365 nm LED light, with a pulse duration of 100 ms. An AxoPatch 200B amplifier (Molecular devices), and Digidata 1550 digitizer (Molecular devices), and Clampex software (Molecular devices), worked together to conduct the measurement and control the light source.

H_2O_2 quantification

Hydrogen Peroxide (H_2O_2) production was evaluated using different concentrations of particles in PBS 5 µg/cm^2. The solutions were added to 24-wells and particles were allowed to settle for 2 hours before being irradiated with 450 nm LED light (75 mW/cm^2), pulsed at 100 ms duration and 1 Hz frequency for 30 minutes. Control groups were kept light-protected under the same conditions. Subsequently, 3x109 µL were transferred from each well to a black 96-well plate. The aliquots were stained with a solution containing 91 µL of horseradish peroxidase (HRP; 4250 units/L, Thermofischer), p-hydroxyphenyl acid (pOHPAA; 1.0e-3 M, Sigma), in 0.25 M Tris buffer (Sigma). Standards with known H_2O_2 concentrations were treated in the same way. Fluorescence intensity was measured with an excitation of 320 nm and an emission of 405 nm using a microplate reader (CLARIOstar Plus Microplate Reader).

Experimental animals

The use of laboratory animals was approved by the Danish Animal Inspectorate (authorization no. 2020-15-0201-00745) and by the Finnish Project Authorization Board (ESAVI/26320/2021). For experiments conducted in Aarhus, eight-week-old C57BL/6JRj male mice were purchased from Janvier Labs (Le Genest-Saint-Isle, France). C57BL/6J mice (n = 3 females, n = 3 males) used at the University of Eastern Finland (UEF) originated from the colony of Lab Animal Centre at UEF. The original colony of the retinitis pigmentosa model B6.CXB1-Pde6brd10/J (RRID: IMSR_JAX:004297, referred to as rd10), mice were a kind gift of Dr. Thierry Leveillard (Sorbonne University) but had been bred as a homozygote line at for at least five generations. In total fourteen rd10 mice were used in this study (n = 5 females and n = 9 males, randomly divided between groups). Animals were maintained under a 12–/12-hour light/dark with free access to autoclaved tap water and standard chow. All procedures were conducted in accordance with the Directive 86/609/EEC for animal experiments, FELASA Guidelines and Recommendations, and ARVO Statement for the Use of Animals in Ophthalmic and Vision Research.

For injections and eye imaging mice were anesthetized with an intraperitoneal injection of a mixture of ketamine and medetomidine (KM) hydrochloride (Ketador or Ketaminol Vet [60–100 mg/kg;, Richter Pharma AG, Wels, Austria; or MSD Animal Health, Espoo, Finland] and Cepetor or Domitor Vet [0.5–1 mg/kg; ScanVet Animal Health A/S, Fredensborg, Denmark; or Orion pharma, Espoo, Finland]). Pupils were dilated with a drop of 1% tropicamide (Mydriacyl; Alcon Nordic A/S, Copenhagen, Denmark), or a mixture of metaoxedrin-tropicamide drops (Oftan Tropicamide, 5mg/ml, Oftan metaoxedrin 100 mg/ml; Santen Oy, Tampere, Finland; mixed in a 1:5 ratio)and eyes lubricated with carbomer eye gel (Viscotears

2 mg/mL, Alcon Nordic). KM anesthesia was reversed by atipamezole 0.5–1 mg/kg (Antisedan, Orion Pharma, Copenhagen, Denmark).

Intravitreal injections

Intravitreal injections (Fig. 7A) were performed under an OPMI 1 FR PRO Surgical microscope (Zeiss, Jena, Germany) or Leica S9D Stereo microscope (Leica Microsystems, Wetzlar, Germany). A 30G disposable needle was used to puncture the sclera near the limbus, and a 33G or a 34G blunt-ended needle connected to a Hamilton syringe (Hamilton Company, Reno, NV, USA) was then inserted into the opening followed by injection of 1 µL hg-C_3N_4 NPs (1 mg/mL), red fluorescent silica particles (sicastar®-Red F, cat# 40-00-101, Micromod, Rostock, Germany), SiO_2 (silica) particles, or PBS buffer solution. In the study with rd10 mice (Fig. 8f-l), Red F and SiO_2 particles were used as controls instead of PBS to more closely mimic the physicochemical nature of hg-C_3N_4 NPs. For the bioavailability and safety study, both eyes of three WT mice were injected with NP solution and one mouse with buffer solution. Seven rd10 mice received hg-C_3N_4 NPs, four mice Red F particles, and three mice received SiO_2 particles bilaterally.

Fundus imaging and optical coherence tomography

Non-invasive fundus imaging was performed at baseline and 14 days following intravitreal injections using the Micron IV image-guided OCT 2 system (Phoenix Research Laboratories, Pleasanton, CA, USA). Cross-sectional OCT B-scans were acquired centered on the optic disc. The images were segmented manually after loading the OCT scans into InSight software (Phoenix Research Laboratories). The coordinates were exported as .csv files and loaded into R (version R-4.3.0). The measurements were recentered around the optic nerve and the distance from the outermost border was calculated. Measurements less than 100 µm and further than 600 µm from the optic disc center were excluded. Mean total retinal thickness, mean NGI-thickness (combined thickness of retinal nerve fiber layer, retinal ganglion cell layer, and inner plexiform layer), mean combined thickness of the inner nuclear layer and outer plexiform layer, and mean outer nuclear layer thickness were calculated for each eye.

Retinal sectioning and flat mounting

Following sacrifice of the animals at day 14 post-injection eyes were enucleated and fixed in 4% stabilized formaldehyde buffer (VWR, Søborg, Denmark) overnight at 4˚C. One eye from each animal was used for flat mounting: The anterior segment and lens were removed and the neuroretina was carefully peeled off the retinal pigment epithelium (RPE)/choroid and immersed in ice-cold PBS buffer before proceeding with immunostaining. The other eye was processed for paraffin embedding and sectioning at the Department of Pathology, Aarhus University Hospital.

Electroretinography

Overnight dark-adapted mice were anesthetized under dim red-light observation with ketamine (60 mg/kg) and medetomidine (0.4 mg/kg) mixture and electroretinography (ERG) was performed as

described before[79]. Only the response for strongest flash (30 cd·s/m^2) was used for analysis.

Light-dark box test

The light-dark box contains a plastic chamber (44 x 18 x 21 cm) divided into two equal compartments by a divider, which had a small passage that allowed animals to move freely between the compartments. One compartment is brightly lit (~ 900 lux) with a lamp above the arena, whereas the other compartment is darkened (~ 5 lux) getting light mostly from the lit side through the passage. Two days before the experimental day, all animals were allowed to familiarize themselves to the test environment for 3 minutes. In the actual experiment, each animal was placed initially in the lit compartment and was allowed to freely move in the apparatus (between the chambers) for 5 minutes in a calm and silent environment. Animal behavior was recorded using a digital camera positioned above the light zone. A researcher blinded as to the treatments analyzed the following behavioral patterns: 1. total time spent in the dark compartment (primary test outcome); 2. number of transitions between the dark and light compartments (measure of the degree of activity).

Cortical visual evoked potentials

Carprofen (20 mg/kg s.c; Rimadyl Vet 50 mg/ml, Zoetis, Helsinki, Finland) was prophylactically administered as a pain killer. Mice were initially anesthetized with isoflurane in an induction chamber (concentration 4.5%) and then transferred to stereotaxic frame (Kopf Instruments, Tujunga, CA, USA) where isoflurane was administered through a nose mask. At this point, also urethane anesthesia (2 g/kg, s.c.) was induced and the pupils were dilated with a mixture of metaoxedrin-tropicamide drops (5mg/ml and 100 mg/ml, respectively, mixed in a 1:5 ratio). During surgical procedures, isoflurane concentration was gradually lowered from 1.5–0.6% until finally stopped (leaving animal to be anesthetized with urethane only) when surgical operations were finalized. The surgery was performed as previously described[80]. The skin over the scalp was locally anesthetized with lidocaine (20 mg/ml, Xylocaine, Aspen Pharma Trading Limited, Irland). Thereafter the scalp was opened with an incision and the skull was cleaned. Holes for electrodes were drilled with a dental drill leaving the dura mater intact. Two stainless steel mini screw (shank diameter 1 mm) were attached on the holes that were drilled bilaterally above the binocular primary visual cortex (medial/lateral: ± 3 mm from lamda), and one on frontal bone (AP: 2 mm; ML: 1 mm) which served as the reference electrodes. The visual evoked potentials (VEPs) were recorded with a Diagnosys Celeris rodent ERG device (Diagnosys LLC, Lowell, MA). The eyes were stimulated one at a time with an ascending (log unit intervals) stimulus intensity series between 0.05 to 500 cd·s/m^2. At least 20 sweeps per stimulus intensity were recorded and averaged. The EEG signal was collected at 2 kHz and bandpass-filtered between 0.25–300 Hz. The VEP amplitude was analyzed from the first negative trough to first positive deflection (both visible in most WT mice), or from the baseline to first positive deflection.

Porcine retina dissection

Eyes from Danish Land Race pigs (*Sus domesticus*) were collected at a local slaughterhouse (Danish Crown, Horsens, Denmark) immediately after the animals had been anesthetized with carbon dioxide and killed by exsanguination. The eyes were transported to Aarhus University Hospital (AUH) laboratory in physiological saline solution (PSS) at 4˚C, and the time from the collection of the eyes to the commencement of the dissection procedure never exceeded 5 h. Dissection was performed in 4˚C PSS0.0 as follows: each eye was bisected at the equator with a double-edged blade, and the anterior segment was removed. The posterior segment containing the optic disc was placed under a stereo microscope, the vitreous body was removed. A few mm from the optic disc a segment of approximately 3 x 3 mm^2 neuroretinal tissue was cut out using a self-locking chisel blade handle (VWR International, Herlev, Denmark) equipped with a 30 microblade (BD Beaver, D.J. Instruments, Billerica, USA). Chemical Solutions for storage and transportation: PSS with the following composition (in mM): 118 NaCl, 4.8 KCl, 1.14 $MgSO_4$, 25 $NaHCO_3$, 5 Hepes, 1.5 $CaCl_2$, 5.5 glucose.

MEA electrophysiology

A micro-electrode array (MEA) with 32 channels from Blackrock Microsystems was used to measure electrical signals from the retinal tissue. The MEA was connected via an Omnetics connector to a Blackrock Microsystems Cereplex Direct dedicated data acquisition. Data was sampled at 30 kHz, high pass filtered at 250 Hz and further filtered for 50 Hz line noise by a built-in Blackrock Line Noise Cancelation filter (filtering 50 Hz, 1 second, soft synchronization). Data was analyzed using custom Matlab software.

After placing the retinal tissue on the MEA with the retinal ganglion cells facing upwards, 5 µg of hg-C_3N_4 NPs dispersed in 20 µL of PBS we added to tissue and allowed to settle for around 15 min. Afterwards, light stimulation was applied using a 450 nm homemade LED system with 1 ms pluses with one pulse per second (1 Hz). The recording length was at least 30 s. The resulting whole data trace for each of the 32 channels were segmented into traces of 1 s duration (minimum 30 traces), initiating at the stimulus artefact. These traces were then averaged in order to improve the signal/noise ratio. All electrophysiological experiments were carried out inside a Faraday cage.

Chemical Solutions for experiments: PSS1.6 with the following composition (in mM): 119 NaCl, 4.7 KCl, 1.17 $MgSO_4$, 25 $NaHCO_3$, 5 Hepes, 1.6 $CaCl_2$, 5.5 glucose, 1.18 KH_2PO_4, 0.026 EDTA. PSS0.0 refers to PSS1.6 where $CaCl_2$ has been omitted.

PSS1.6 was heated to 37˚C and oxygenated prior to all experiments in order to ensure a physiological environment during electrical measurements. Tetrodotoxin (TTX) citrate was obtained from Hello Bio Reagents (Bristol, United Kingdom, HB1035). TTX solutions were prepared by creating a stock solution of TTX in PSS1.6 of 1.0 M concentration. From this solution 1 mL aliquots of 2.25 mM concentration were created for use in future experiments. All TTX solutions were stored at -20˚C between experiments. For TTX control experiments, a volume of 50 µL of the TTX solution was applied directly to the tissue sample.

NP uptake and ex vivo culture of porcine retina

Porcine eyes were obtained from the slaughterhouse as described previously. Periocular tissue was removed, and the eye was disinfected in a 10% w/v iodine solution (polyvinylpyrrolidone-iodine complex [Thermo Fisher Scientific, Roskilde, Denmark] in PBS). The anterior segment of the eye was cut off and blunt forceps were used to remove the vitreous. The remaining tissue was quartered and for each a 6 mm punch out of the retina was carefully transferred to a well with 1:1 DMEM/F12 (both Euroclone, Pero, MI, Italy) medium supplemented with 2% B-27 (Thermo Fisher Scientific), 1 µg/mL streptomycin, 1 U/mL penicillin, and 2 mM L-glutamine (all Euroclone). Media was aspirated and 30 µL NP solution (2 mg/mL) was added directly onto the retinas and incubated for 30 minutes. Afterwards media was added, and retinas incubated for 24 hours.

Immunostaining of retinal flat mounts and sections

Porcine retinaswere fixed for 6 hours at RT in 4% stabilized formaldehyde buffer (VWR), washed three times in PBS, and blocked and permeabilized overnight at 4˚C in retina blocking buffer (RBB) containing PBS with 1% BSA (VWR) and 0.5% Triton X100 (Sigma, Søborg, Denmark). Next, retinas were incubated with rabbit anti-RbPMS (RNA binding protein with multiple splicing, RGC marker) (1.6 mg/mL; NBP2-20112, Novus Biologicals, Littleton, ON, Canada) diluted 1:500 for 48 hours at 4˚C. Following wash in wash buffer (PBS with 0.5% Triton X100) they were incubated with Alexa-568 Donkey anti-rabbit (2 mg/mL; A10042, Thermo Fisher Scientific) diluted 1:400 overnight at 4˚C). Retinas were then washed and counterstained with Draq5 (5 mM; 62251, Thermo Fisher Scientific) diluted 1:1000 in PBS for 10 minutes. Finally, retinas were washed and transferred to glass slides, where they were mounted with the RGC layer facing upwards using Fluoromount-G mounting medium (Thermo Fisher Scientific).

Mouse flat mounts were blocked and permeabilized overnight at 4°C in RBB before being incubated with rabbit anti-RbPMS (1.6 mg/mL; NBP2-20112, Novus Biologicals) diluted 1:400 in RBB overnight at 4˚C. Next, the retinas were washed and incubated with Alexa-568 goat anti-rabbit (2 mg/mL; A11011, Thermo Fisher Scientific) diluted 1:400 in RBB overnight at 4˚C. The flat mounts were washed and counterstained with Draq5 (5 mM; 62251, Thermo Fisher Scientific) diluted 1:1000 in wash buffer before they were transferred to glass slides and mounted with the RGC layer facing upwards using Fluoromount-G mounting medium (Thermo Fisher Scientific).

Mouse retinal sections were deparaffinized in xylene overnight before rehydration with graded ethanol washes. Heat-induced epitope retrieval was performed in citrate buffer pH 6. Sections were blocked with 3% BSA and 1% Triton X100 in PBS for 1 hour before incubation with anti-RbPMS (1 mg/mL; NBP2-20112, Novus Biologicals) diluted 1:400 in PBS with 1% BSA overnight at 4˚C. The next day, sections were washed and incubated with Alexa-488 goat anti-rabbit (2 mg/mL; A11008, Thermo Fisher Scientific) diluted 1:400 in PBS with 1% BSA for 30 minutes. The sections were washed and counterstained with Draq5 (5 mM; 62251, Thermo Fisher Scientific) diluted 1:1000 in PBS and mounted with Fluoromount-G mounting medium (Thermo Fisher Scientific) on glass slides.

Imaging of retinal sections

Image acquisition and analyses were performed at the Bioimaging Core Facility, Health, Aarhus University, Denmark. Retinal sections were imaged with the Olympus VS120 upright widefield fluorescence microscope (Olympus, Tokyo, Japan) equipped with Spectra X 7IR LED multi-spectral light engine and Semrock pentafilter (DAPI/FITC/Cy3/Cy5/Cy7 Penta LED HC Filter Set #F68-050) with Hamamatsu ORCA-FLASH4.0 V2 (QE 82%) camera (Hamamatsu, Shizuoka, Japan). Overview images were taken with the Olympus UPlanSApo 20x/0.75 air objective and associated VS-ASW imaging software.

Retinal sections and flat mounts were imaged with a Zeiss LSM 800 confocal laser scanning microscope (Zeiss, Jena, Germany) using a Plan-Apochromat 63x/1.4 oil objective. Excitation and emission wavelengths were λex = 405 nm and λem = 400–605 nm for the DAPI channel, λex = 488 nm and λem = 400–650 nm for Alexa Fluor 488, λex = 561 and λem = 400–650 for Alexa Fluor 568, and λex = 640 and λem = 650–700 for the Cy5 channel.

Images were captured with fixed settings and processed similarly. Display settings are similar and fluorescence intensities are comparable among images in the same figure.

Statistical analysis

Statistical analysis was performed in GraphPad Prism 9.3.1. The analysis was performed using either unpaired two-tailed t-test or one-way ANOVA and Tukey's test for multiple comparisons where $p < 0.0001$ is denoted as ****. Comparison of retinal layers was performed using R (version R-4.3.0) using paired two-tailed t-tests.

Declarations

Acknowledgments

M. Chen gratefully acknowledges the Carlsberg Foundation (CF19-0300) for supporting this work. B. Tian acknowledges the support from the Ziyi-Zhong gift. T. Bek, J. G. Madsen and R. S. Davidsen gratefully acknowledge the Novo Nordisk Foundation (NNF20OC0064628,). T. Bek and T.J. Corydon acknowledges the APT Holding. H. Leinonen acknowledges support from the Research Council of Finland, Business Finland, Emil Aaltonen Foundation, Sigrid Jusélius Foundation, Päivikki and Sakari Sohlberg Foundation, Finnish Eye and Tissue Bank Foundation, Retina Registered Association (Finland), and Sokeain Ystävät/De Blindas Vänner Registered Association. T.J. Corydon acknowledges the VELUX Foundation (Grant No. 00038189), and the Independent Research Fund Denmark (Grant No. 2034-00036B). A.L. Askou gratefully acknowledges The Danish Eye Research Foundation. T.S. Jakobsen acknowledges Fight for Sight, Denmark and the Synoptik Foundation. Fig. 1 and 5a were partly generated using Servier Medical Art, provided by Servier, licensed under a Creative Commons Attribution 3.0 unported license. The authors acknowledge the Bioimaging Core Facility, Department of Biomedicine, Aarhus University,

Denmark, for the use of equipment and support. The authors thank Tina Hindkjær for excellent technical assistance.

Funding:

Carlsberg Foundation (CF19-0300)

Ziyi-Zhong gift

Novo Nordisk Foundation (NNF20OC0064628)

APT Holding

VELUX Foundation (00038189)

Independent Research Fund Denmark (2034-00036B)

Fight for Sight

The Danish Eye Research Foundation

Synoptik Foundation

Author contributions:

Conceptualization: MC, BT, CAM

Methodology: MC, BT, HL, CAM, LM, WL, TSJ, ALA, TJC

Investigation: CAM, YZ, LM, JGM, KKK, TSJ, ACJ, AA, AK,GH, TSJ, ALA

Visualization: MC, HL, CAM, YZ, TSJ, ALA

Supervision: MC, BT, TB, MD, RSD, TJC, NSH, ALA

Writing-original draft: CAM, CM, BT, TB, JGM, RSD, MD, TSJ, ALA, TJC

Competing interests: The authors declare that they have no competing interests.

Data and materials availability:

All data needed to evaluate the conclusions in the paper are present in the paper and/or the Supplementary Materials. Additional data related to this paper may be requested from the authors.

References

1. Famm, K., Litt, B., Tracey, K. J., Boyden, E. S. & Slaoui, M. A jump-start for electroceuticals. *Nature***496**, 159-161 (2013).
2. Powell, M. P. *et al.* Epidural stimulation of the cervical spinal cord for post-stroke upper-limb paresis. *Nature Medicine*, 1-11 (2023).
3. Rochford, A. E. *et al.* Functional neurological restoration of amputated peripheral nerve using biohybrid regenerative bioelectronics. *Science Advances***9**, eadd8162 (2023).
4. Cox-Pridmore, D. M., Castro, F. A., Silva, S. R. P., Camelliti, P. & Zhao, Y. Emerging bioelectronic strategies for cardiovascular tissue engineering and implantation. *Small***18**, 2105281 (2022).
5. Wellman, S. M. *et al.* A materials roadmap to functional neural interface design. *Advanced functional materials***28**, 1701269 (2018).
6. Bansal, A., Shikha, S. & Zhang, Y. Towards translational optogenetics. *Nature Biomedical Engineering*, 1-21 (2022).
7. Maimon, B. E. *et al.* Optogenetic peripheral nerve immunogenicity. *Scientific reports***8**, 14076 (2018).
8. Marino, A. *et al.* Piezoelectric nanoparticle-assisted wireless neuronal stimulation. *ACS nano***9**, 7678-7689 (2015).
9. Parameswaran, R. *et al.* Photoelectrochemical modulation of neuronal activity with free-standing coaxial silicon nanowires. *Nature nanotechnology***13**, 260-266 (2018).
10. Zimmerman, J., Parameswaran, R. & Tian, B. Nanoscale semiconductor devices as new biomaterials. *Biomaterials science***2**, 619-626 (2014).
11. Li, P. *et al.* Monolithic silicon for high spatiotemporal translational photostimulation. 1-9 (2024).
12. Johnson, A., Lewis, J. & ALBERTS, B. Molecular biology of the cell. (2002).
13. Shang, L. & Nienhaus, G. U. Small fluorescent nanoparticles at the nano–bio interface. *Materials Today***16**, 58-66 (2013).
14. Maya-Vetencourt, J. F. *et al.* Subretinally injected semiconducting polymer nanoparticles rescue vision in a rat model of retinal dystrophy. *Nature nanotechnology***15**, 698-708 (2020).
15. Wang, Y., Garg, R., Cohen-Karni, D. & Cohen-Karni, T. Neural modulation with photothermally active nanomaterials. *Nature Reviews Bioengineering***1**, 193-207 (2023).
16. Bahmani Jalali, H. *et al.* Biocompatible quantum funnels for neural photostimulation. *Nano letters***19**, 5975-5981 (2019).
17. Chen, L. *et al.* Ultrathin 2D Graphitic Carbon Nitride on Metal Films: Underpotential Sodium Deposition in Adlayers for Sodium-Ion Batteries. *Angewandte Chemie International Edition***59**, 9067-9073 (2020).
18. Kessler, F. K. *et al.* Functional carbon nitride materials—design strategies for electrochemical devices. *Nature Reviews Materials***2**, 1-17 (2017).
19. Liao, G. *et al.* Emerging graphitic carbon nitride-based materials for biomedical applications. *Progress in Materials Science***112**, 100666 (2020).

20. Müller, C. A. *et al.* Bionic Opto-responsive Fiber for Directing Neurite Growth. *Materials Today Nano*, 100311 (2023).
21. Zhang, Z. Y. *et al.* 3D anisotropic photocatalytic architectures as bioactive nerve guidance conduits for peripheral neural regeneration. *Biomaterials***253** (2020). https://doi.org/ARTN 120108 10.1016/j.biomaterials.2020.120108
22. Zhang, Z. Y. *et al.* Visible-Light Neural Stimulation on Graphitic-Carbon Nitride/Graphene Photocatalytic Fibers. *Acs Appl Mater Inter***9**, 34736-34743 (2017). https://doi.org/10.1021/acsami.7b12733
23. Sun, J. *et al.* Bioinspired hollow semiconductor nanospheres as photosynthetic nanoparticles. *Nature Communications***3**, 1139 (2012).
24. Hu, G. P., Huang, J. B. & Fussenegger, M. Toward Photosynthetic Mammalian Cells through Artificial Endosymbiosis. *Small***20** (2024). https://doi.org/10.1002/smll.202310310
25. Jiang, Y. & Tian, B. Inorganic semiconductor biointerfaces. *Nature Reviews Materials***3**, 473-490 (2018).
26. Jiang, Y. *et al.* Nongenetic optical neuromodulation with silicon-based materials. *Nature protocols***14**, 1339-1376 (2019).
27. Gentemann, L. *et al.* Modulation of cardiomyocyte activity using pulsed laser irradiated gold nanoparticles. *Biomedical optics express***8**, 177-192 (2017).
28. Gholami Derami, H. *et al.* Reversible photothermal modulation of electrical activity of excitable cells using polydopamine nanoparticles. *Advanced Materials***33**, 2008809 (2021).
29. Parameswaran, R. *et al.* Optical stimulation of cardiac cells with a polymer-supported silicon nanowire matrix. *Proceedings of the National Academy of Sciences***116**, 413-421 (2019).
30. Lavoie-Cardinal, F., Salesse, C., Bergeron, É., Meunier, M. & De Koninck, P. Gold nanoparticle-assisted all optical localized stimulation and monitoring of Ca2+ signaling in neurons. *Scientific reports***6**, 20619 (2016).
31. Lendahl, U., Muhl, L. & Betsholtz, C. Identification, discrimination and heterogeneity of fibroblasts. *Nature Communications***13**, 3409 (2022).
32. Klesen, A. *et al.* Cardiac fibroblasts. *Herzschrittmachertherapie + Elektrophysiologie***29**, 62-69 (2018). https://doi.org/10.1007/s00399-018-0553-3
33. Zhao, M. *et al.* Electrical signals control wound healing through phosphatidylinositol-3-OH kinase-γ and PTEN. *Nature***442**, 457-460 (2006).
34. Krassovka, J. M. *et al.* The impact of non-toxic blue light (453 nm) on cellular antioxidative capacity, TGF-β1 signaling, and myofibrogenesis of human skin fibroblasts. *Journal of Photochemistry and Photobiology B: Biology***209**, 111952 (2020).
35. Gimondi, S., de Castro, J. V., Reis, R. L., Ferreira, H. & Neves, N. M. On the size-dependent internalization of sub-hundred polymeric nanoparticles. *Colloids and Surfaces B: Biointerfaces***225**, 113245 (2023).

36. Zhao, W. *et al.* Nanoscale manipulation of membrane curvature for probing endocytosis in live cells. *Nature nanotechnology***12**, 750-756 (2017).
37. Blechinger, J. *et al.* Uptake kinetics and nanotoxicity of silica nanoparticles are cell type dependent. *Small***9**, 3970-3980 (2013).
38. Zhang, Y., Hu, L., Yu, D. & Gao, C. Influence of silica particle internalization on adhesion and migration of human dermal fibroblasts. *Biomaterials***31**, 8465-8474 (2010).
39. Zimmerman, J. F. *et al.* Cellular uptake and dynamics of unlabeled freestanding silicon nanowires. *Science advances***2**, e1601039 (2016).
40. Chilton, L. *et al.* K+ currents regulate the resting membrane potential, proliferation, and contractile responses in ventricular fibroblasts and myofibroblasts. *American Journal of Physiology-Heart and Circulatory Physiology***288**, H2931-H2939 (2005).
41. Kamkin, A. *et al.* Characterization of stretch-activated ion currents in isolated atrial myocytes from human hearts. *Pflügers Archiv***446**, 339-346 (2003).
42. Chilton, L. *et al.* K+ currents regulate the resting membrane potential, proliferation, and contractile responses in ventricular fibroblasts and myofibroblasts. *Am J Physiol-Heart C***288**, H2931-H2939 (2005). https://doi.org/10.1152/ajpheart.01220.2004
43. Kamkin, A. *et al.* Characterization of stretch-activated ion currents in isolated atrial myocytes from human hearts. *Pflug Arch Eur J Phy***446**, 339-346 (2003). https://doi.org/10.1007/s00424-002-0948-0
44. Pellman, J., Zhang, J. & Sheikh, F. Myocyte-fibroblast communication in cardiac fibrosis and arrhythmias: Mechanisms and model systems. *J Mol Cell Cardiol***94**, 22-31 (2016). https://doi.org/10.1016/j.yjmcc.2016.03.005
45. Klesen, A. *et al.* Cardiac fibroblasts : Active players in (atrial) electrophysiology? *Herzschrittmacherther Elektrophysiol***29**, 62-69 (2018). https://doi.org/10.1007/s00399-018-0553-3
46. Zhang, Y., Le Friec, A., Sun, D. & Chen, M. Sinusoidal stretchable fibrous electrodes regulate cardiac contraction. *Chemical Engineering Journal***455**, 140555 (2023).
47. Yue, L., Weiland, J. D., Roska, B. & Humayun, M. S. Retinal stimulation strategies to restore vision: Fundamentals and systems. *Progress in retinal and eye research***53**, 21-47 (2016).
48. Chang, B. *et al.* Two mouse retinal degenerations caused by missense mutations in the β-subunit of rod cGMP phosphodiesterase gene. *Vision Res***47**, 624-633 (2007). https://doi.org/10.1016/j.visres.2006.11.020
49. Leinonen, H. & Tanila, H. Vision in laboratory rodents-Tools to measure it and implications for behavioral research. *Behav Brain Res***352**, 172-182 (2018). https://doi.org/10.1016/j.bbr.2017.07.040
50. Bourin, M. & Hascoët, M. The mouse light/dark box test. *Eur J Pharmacol***463**, 55-65 (2003). https://doi.org/10.1016/S0014-2999(03)01274-3
51. Wagner, N. *et al.* Novel porcine retina cultivation techniques provide improved photoreceptor preservation. *Frontiers in Neuroscience***14**, 556700 (2020).

52. Bakkum, D. J. *et al.* Tracking axonal action potential propagation on a high-density microelectrode array across hundreds of sites. *Nature communications***4**, 2181 (2013).
53. Tong, W., Meffin, H., Garrett, D. J. & Ibbotson, M. R. Stimulation strategies for improving the resolution of retinal prostheses. *Frontiers in neuroscience***14**, 262 (2020).
54. Katikou, P., Gokbulut, C., Kosker, A. R., Campàs, M. & Ozogul, F. An updated review of tetrodotoxin and its peculiarities. *Marine Drugs***20**, 47 (2022).
55. Hausmann, D. *et al.* Autonomous rhythmic activity in glioma networks drives brain tumour growth. *Nature***613**, 179-186 (2023).
56. Xu, D., Mo, J., Xie, X. & Hu, N. In-cell nanoelectronics: opening the door to intracellular electrophysiology. *Nano-Micro Letters***13**, 127 (2021).
57. Li, P. J. *et al.* Monolithic silicon for high spatiotemporal translational photostimulation. *Nature* (2024). https://doi.org/10.1038/s41586-024-07016-9
58. Jin, H., Heller, D. A. & Strano, M. S. Single-particle tracking of endocytosis and exocytosis of single-walled carbon nanotubes in NIH-3T3 cells. *Nano letters***8**, 1577-1585 (2008).
59. Guo, S. *et al.* Selectivity of commonly used inhibitors of clathrin-mediated and caveolae-dependent endocytosis of G protein–coupled receptors. *Biochimica et Biophysica Acta (BBA)-Biomembranes***1848**, 2101-2110 (2015).
60. Rotenberg, M. Y. *et al.* Silicon nanowires for intracellular optical interrogation with subcellular resolution. *Nano letters***20**, 1226-1232 (2020).
61. Liu, J. *et al.* Genetically targeted chemical assembly of functional materials in living cells, tissues, and animals. *Science***367**, 1372-1376 (2020).
62. Nair, V. *et al.* Laser writing of nitrogen-doped silicon carbide for biological modulation. *Science Advances***6**, eaaz2743 (2020).
63. Wu, T.-H., Teslaa, T., Teitell, M. A. & Chiou, P.-Y. Photothermal nanoblade for patterned cell membrane cutting. *Optics express***18**, 23153-23160 (2010).
64. Steinbach, A. M. *et al.* The Electronic Properties of Silicon Nanowires during Their Dissolution under Simulated Physiological Conditions. *Applied Sciences***9**, 804 (2019).
65. Zhao, Y. *et al.* Mechanistic analysis of multiple processes controlling solar-driven H2O2 synthesis using engineered polymeric carbon nitride. *Nature Communications***12**, 3701 (2021).
66. Sies, H. *et al.* Defining roles of specific reactive oxygen species (ROS) in cell biology and physiology. *Nature Reviews Molecular Cell Biology*, 1-17 (2022).
67. Gamper, N. & Ooi, L. Redox and nitric oxide-mediated regulation of sensory neuron ion channel function. *Antioxidants & redox signaling***22**, 486-504 (2015).
68. Abdullaeva, O. S. *et al.* Faradaic Pixels for Precise Hydrogen Peroxide Delivery to Control M-Type Voltage-Gated Potassium Channels. *Advanced Science***9**, 2103132 (2022).
69. Kimura, H. *et al.* Toxicity and roles of reactive oxygen species. *Current Drug Targets-Inflammation & Allergy***4**, 489-495 (2005).

70. Mohammad-Beigi, H. *et al.* Tracing the in vivo fate of nanoparticles with a “non-self” biological identity. *ACS nano***14**, 10666-10679 (2020).
71. Zhang, Q., Liu, X., Chaker, M. & Ma, D. Advancing graphitic carbon nitride-based photocatalysts toward broadband solar energy harvesting. *ACS Materials Letters***3**, 663-697 (2021).
72. Kuang, X. *et al.* Self-enhancing sono-inks enable deep-penetration acoustic volumetric printing. *Science***382**, 1148-1155 (2023). https://doi.org/10.1126/science.adi1563
73. Wang, R. C., Lin, Y. C., Chen, H. C. & Lin, W. Y. Energy harvesting from g-C N piezoelectric nanogenerators. *Nano Energy***83** (2021). https://doi.org/ARTN 105743 10.1016/j.nanoen.2021.105743
74. Thermoscientific. Pierce Primary Cardiomyocyte Isolation Kit. (2016).
75. Daniel B. Allan, T. C., Nathan C. Keim, and Casper M. van der Wel. <https://zenodo.org/record/1226458> (2018).
76. Crocker, J. C., Grier, D. G. J. J. o. c. & science, i. Methods of digital video microscopy for colloidal studies. **179**, 298-310 (1996).
77. Pasqualin, C. *et al.* Spiky: An ImageJ Plugin for Data Analysis of Functional Cardiac and Cardiomyocyte Studies. *Journal of Imaging***8**, 95 (2022).
78. dFoFmovie-CatFullAutoSave.java (Github, 2014).
79. Pazur, E. J. *et al.* Synthesis and Biological Analysis of Iso-dimethyltryptamines in a Model of Light-Induced Retinal Degeneration. *Acs Med Chem Lett* (2024). https://doi.org/10.1021/acsmedchemlett.4c00130
80. Singh, Y. *et al.* Loss of leads to altered expression and deficits in interneuron development in mice. *Hum Mol Genet***28**, 3309-3322 (2019). https://doi.org/10.1093/hmg/ddz165

Figures

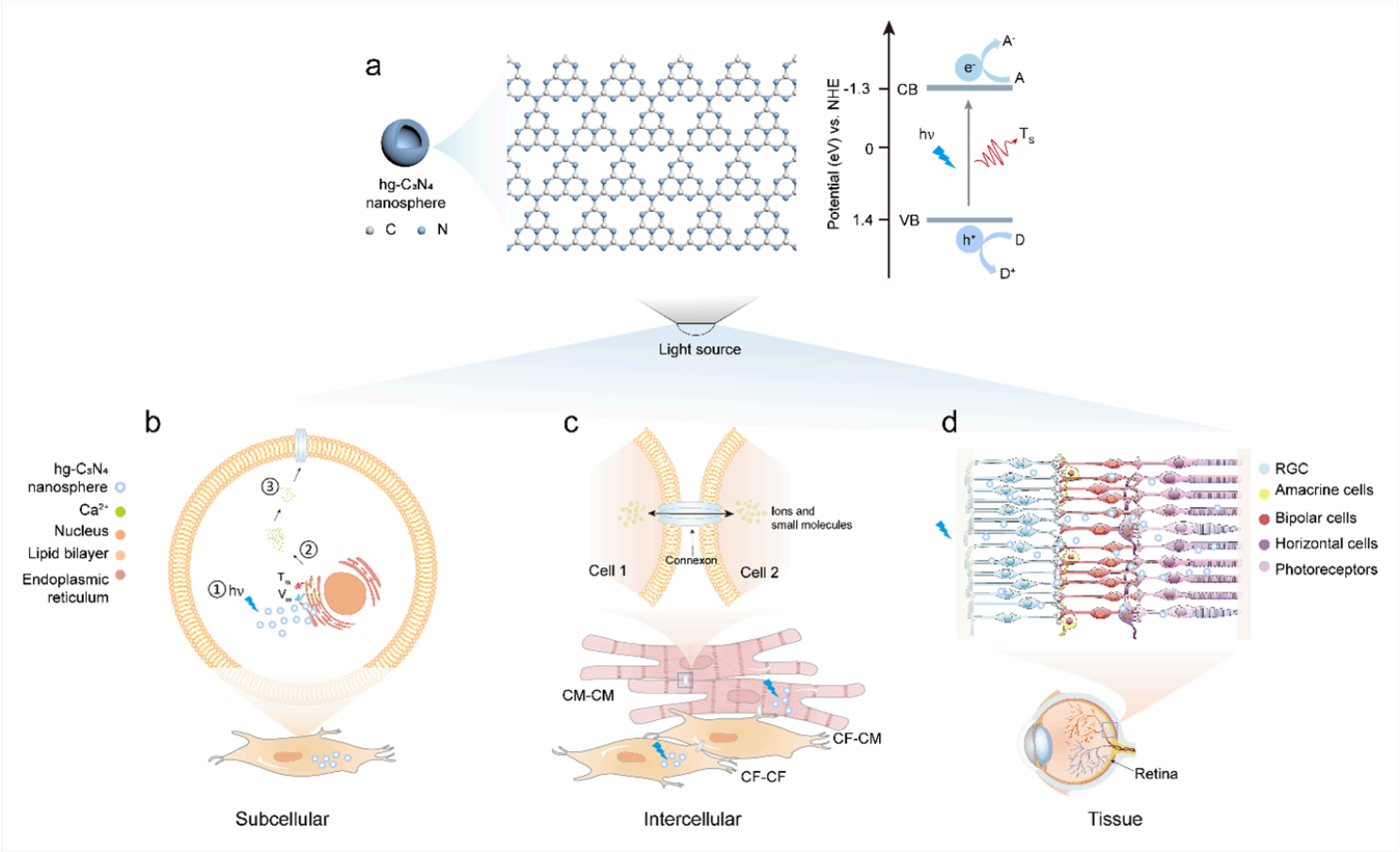

Figure 1

Schematic of hg-C_3N_4 NPs for versatile multiscale optical biomodulation. (a) The chloroplast mimicking hollow sphere (hg-C_3N_4) NPs with chemical structure consisting of a covalent triazine network. The bandgap diagram indicates electrons reacting with acceptor (A) compounds and holes reacting with donator (D) compounds, while simultaneously inducing photothermal heating (T_s). **(b)** Proposed mechanism of optical stimulation with subcellular resolution, where photostimulation of hg-C_3N_4 NPs leads to injection of faradaic photocurrent and photothermal heating, interacting with membrane of calcium storing organelle (1), and membrane depolarization (2) leads to intracellular calcium flux through the cytosol (3). **(c)** Photostimulation of hg-C_3N_4 NPs facilitates intercellular electrophysiological interaction of cardiac fibroblast (CF) and cardiomyocytes (CM). **(d)** hg-C_3N_4 NPs as injectable retina prosthesis stimulating retinal ganglion cells upon photostimulation.

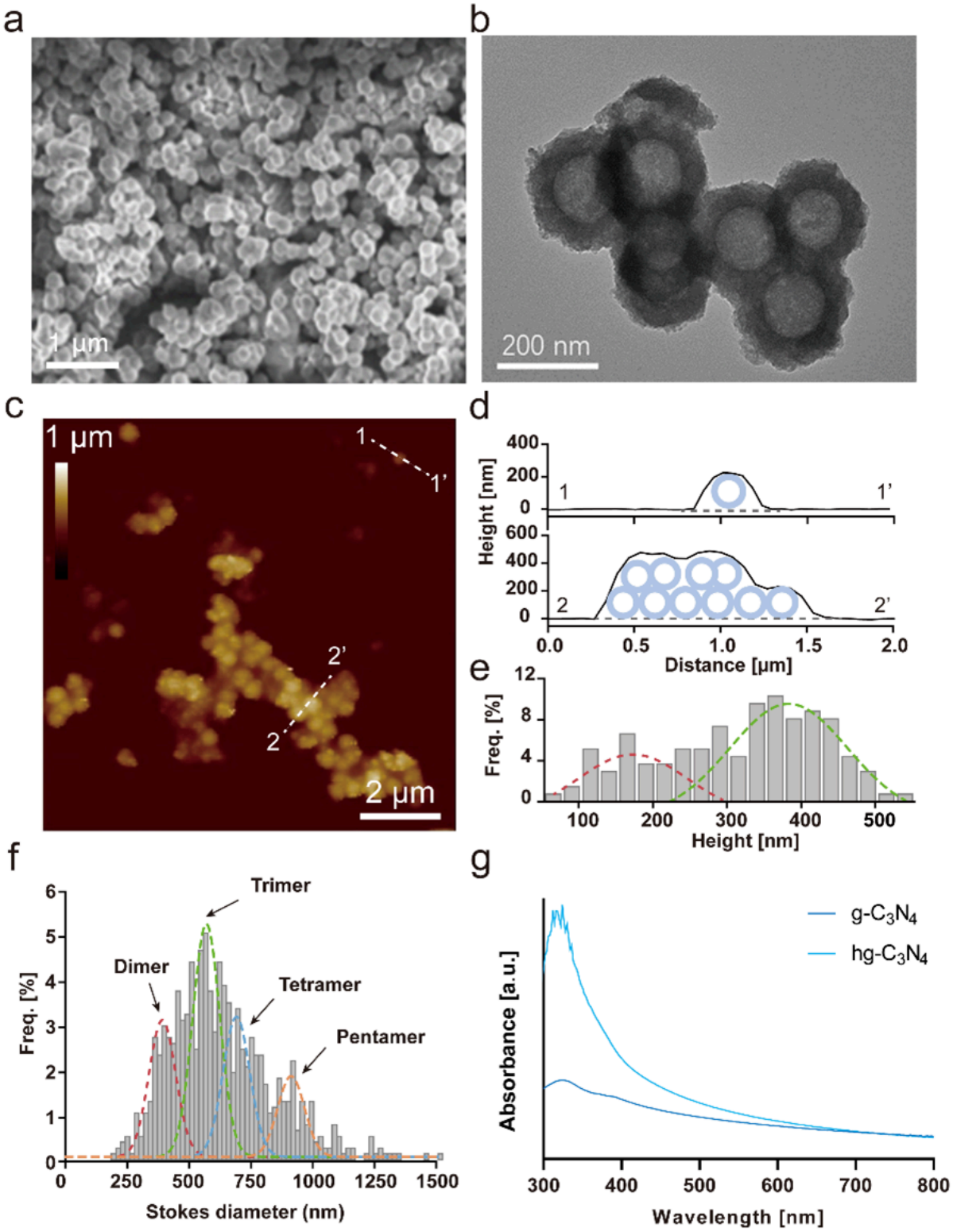

Figure 2

Characterization of hg-C_3N_4 NPs. SEM (**a**) and TEM (**b**) image of hg-C_3N_4 NPs. AFM topographical image (**c**) with corresponding height line profile (**d**) of single hg-C_3N_4 NPs (1-1') and aggregated hg-C_3N_4 NPs (2-2'). **(e)** Particle height distribution of **(c)**. **(f)** Stokes diameter distribution derived from particle tracking analysis of hg-C_3N_4 NPs. **(g)** UV-vis absorption spectrum of hg-C_3N_4 and bulk g-C_3N_4.

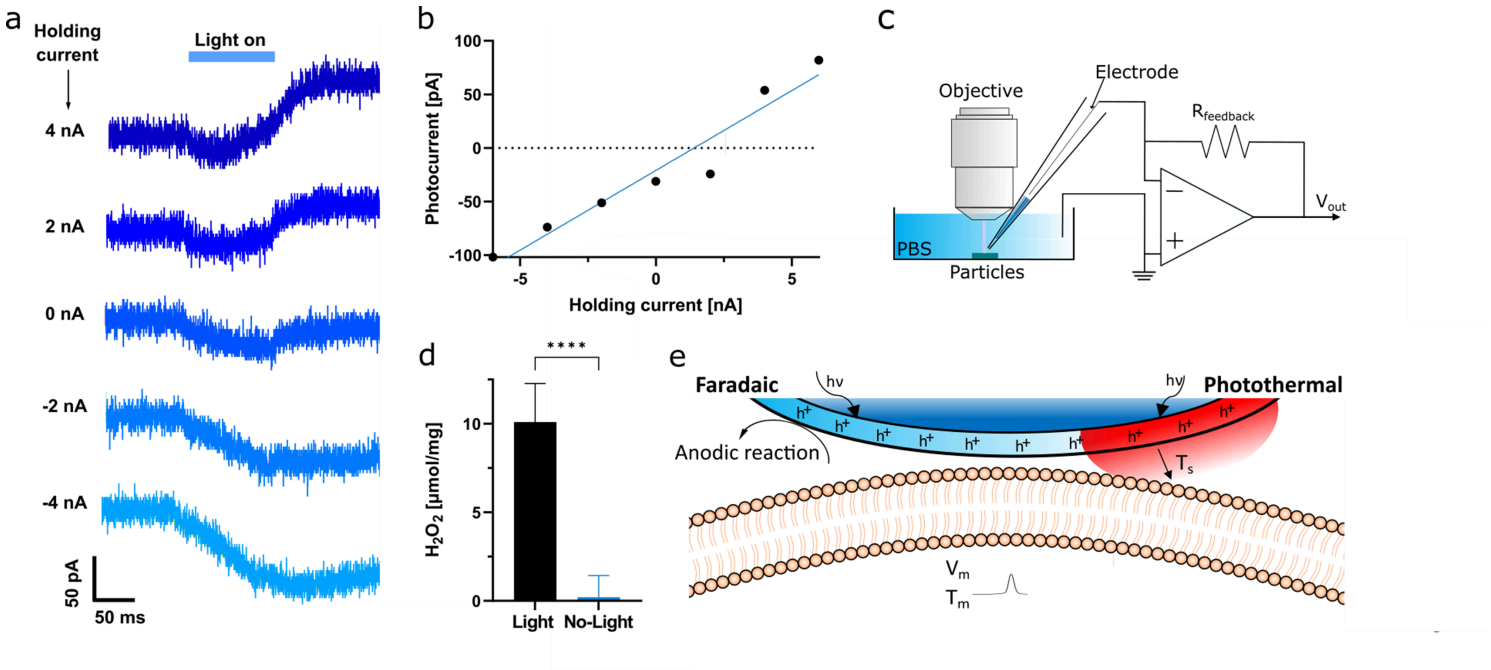

Figure 3

Photocurrent characterization. **(a)** Photocurrent traces measured for a range of holding currents I_0 while applying 100 ms LED illumination. (**b**) Photocurrent amplitude for a range of holding currents 100 ms LED illumination. **(c)** Illustration of patch-clamp photo-response measurement set-up used to measure photocurrent. **(d)** Quantification of hg-C_3N_4 NPs produced H_2O_2 under visible-light LED illumination. Data (n=7) is shown as means ± s.d. Statistical analysis was perfomed using unpaired two-tailed t-test where $p<0.0001$ is denoted as ****. **(e)** Proposed hg-C_3N_4 NPs stimulation mechanism based on anodic faradaic photocurrent and photothermal effect affecting adjacent cell membrane by altering the transmembrane potential (V_m) or increasing temperature of the cell membrane (T_m), respectively. T_s, light-induced heating; hv, photon energy.

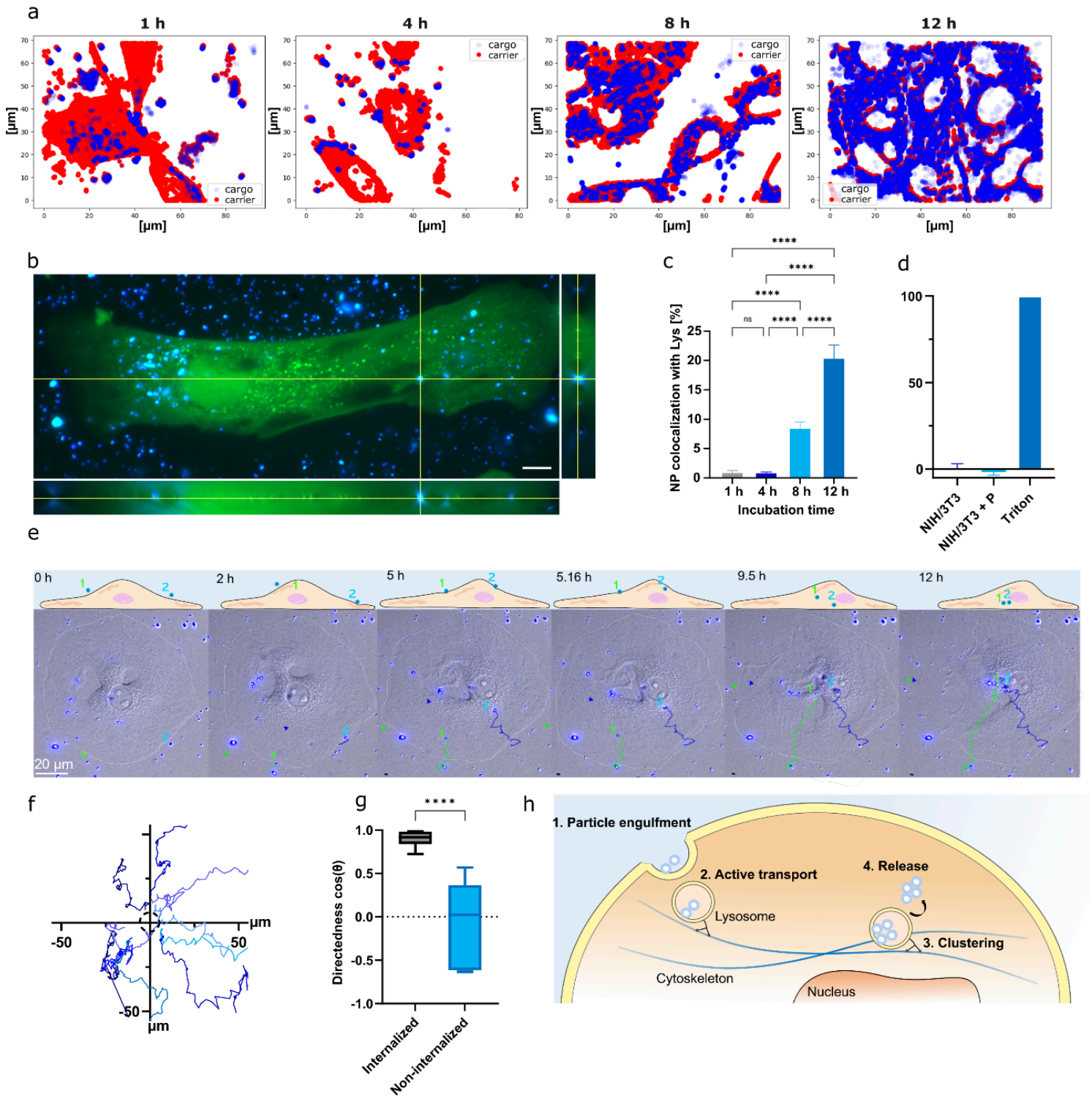

Figure 4

Internalization and cytocompatibility of hg-C_3N_4 NPs. **(a)** The 2D location of Lys (carrier, red) with hg-C_3N_4 NPs (cargo, blue) in NIH/3T3 fibroblasts recorded based on spinning disk confocal microscope (200 frames overlap). **(b)** Z-stack of single NIH/3T3 cell with internalized blue fluorescent hg-C_3N_4 NPs. Green is viability marker. Scale bar is 10 µm. **(c)** Quantification of colocalization of Lys with hg-C_3N_4 NPs in NIH/3T3. Data shown as means ± s.d. (n=200). Statistical analysis was perfomed with one-way ANOVA where $p<0.0001$ is denoted as ****. **(d)** LDH cytotoxicity assay. Data (n=6) is shown as means ±

s.d. **(e)** Tracking of two representative particles internalized by NIH/3T3 cell. **(f)** Particle tracking of 11 internalized particles over 16h. Dashed circle in the middle represents nucleus. **(g)** Quantification of directedness of internalized and non-internalized particles shown as boxplots (n=8). Statistical analysis was performed using unpaired two-tailed t-test where p<0.0001 is denoted as ****. **(h)** Scheme of proposed internaliztaion mechanism.

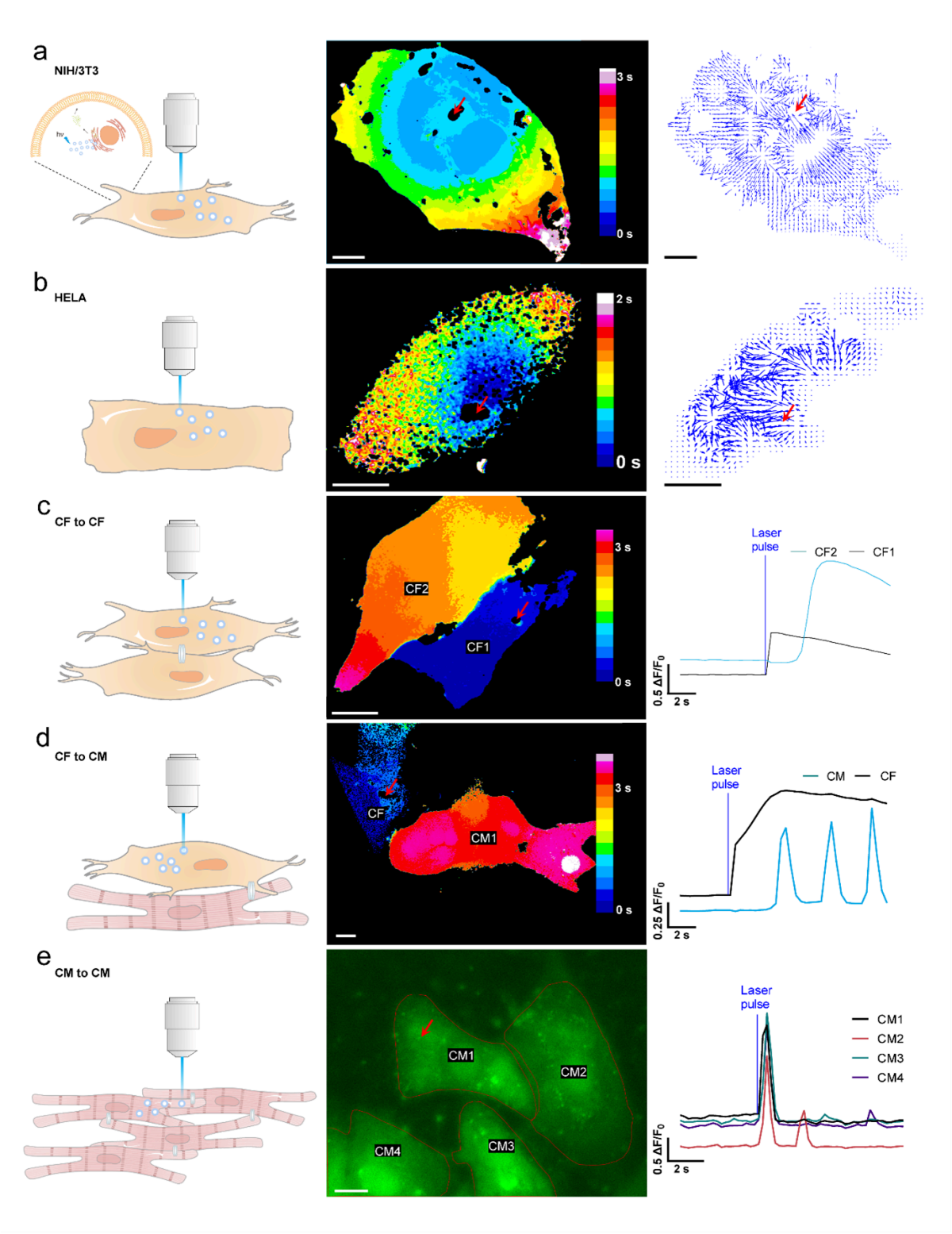

Figure 5

Subcellular and intercellular electrical interrogation. Intracellular electrical interrogation of NIH/3T3 fibroblast **(a)** and HELA cell (**b**) with corresponding isochromal and vector map. Inset in (**a**) shows the proposed calcium release mechanism based on calcium storing ER. **(c)** Intercellular calcium propagation with corresponding isochromal maps or caclium staining with $\Delta F/F_0$ plots between CFs, CF and CM (**d**), CM and CM (**e**). Scale bars are 10 µm. Red arrow indicates location of 200 ms laser pulse, 473 nm, spot size 3 µm, 8.8 mW/µm^2.



Figure 6

. The 2D location of Lys (carrier, red) with hg-CN NPs (cargo, blue) in NIH/3T3 fibroblasts recorded based on spinning disk confocal microscope (200 frames overlap). Z-stack of single NIH/3T3 cell with internalized blue fluorescent hg-CN NPs. Green is viability marker. Scale bar is 10 µm. Quantification of colocalization of Lys with hg-CN NPs in NIH/3T3. Data shown as means ± s.d. (n = 200). Statistical analysis was perfomed with one-way ANOVA where $p < 0.0001$ is denoted as ****. LDH cytotoxicity assay. Data (n = 6) is shown as means ± s.d. Tracking of two representative particles internalized by NIH/3T3 cell. Particle tracking of 11 internalized particles over 16h. Dashed circle in the middle represents nucleus. Quantification of directedness of internalized and non-internalized particles shown as boxplots (n = 8). Statistical analysis was performed using unpaired two-tailed t-test where $p < 0.0001$ is denoted as ****. Scheme of proposed internaliztaion mechanism.

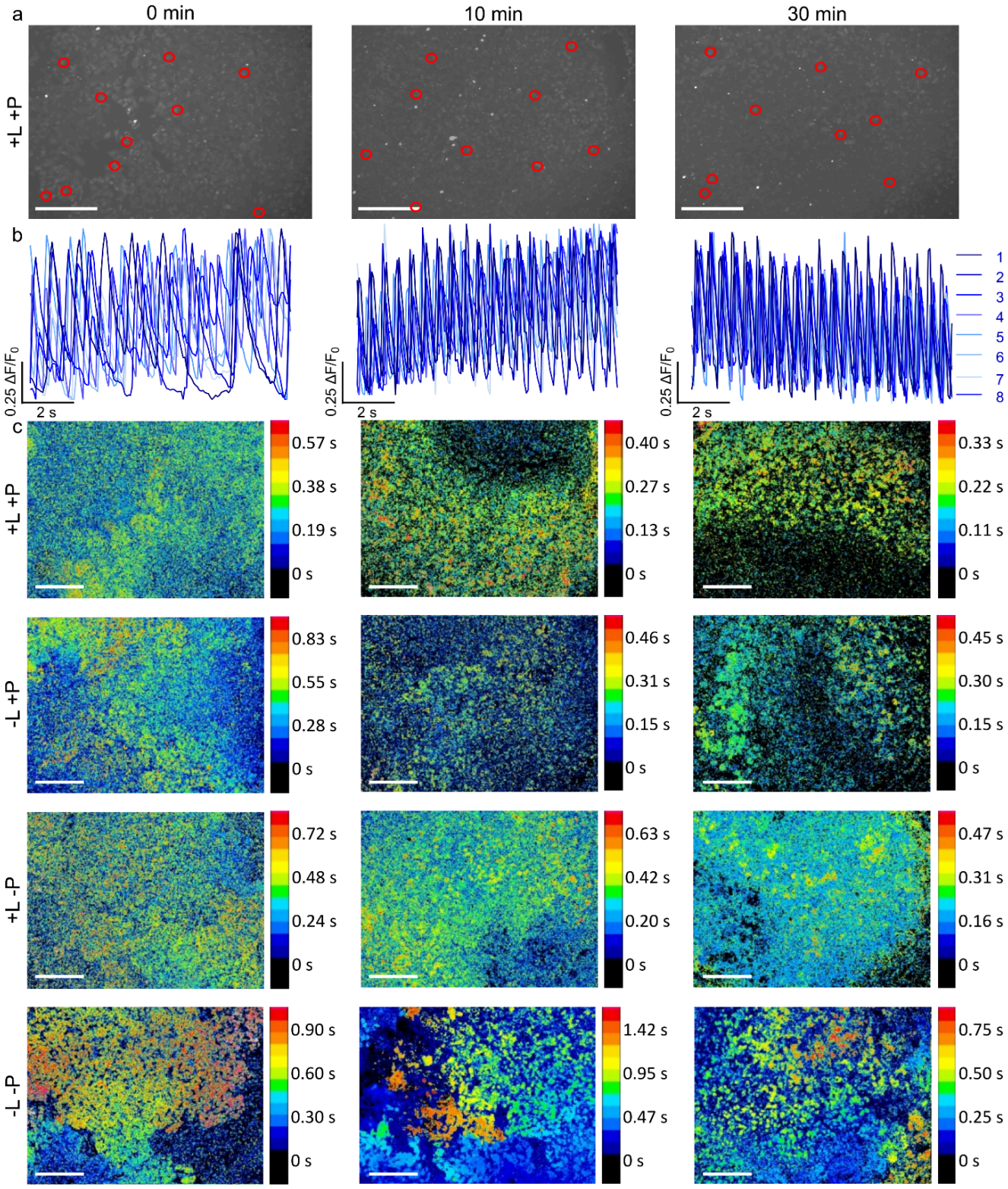

Figure 6

Pacing of cardiomyocyte via photostimulation of hg-C_3N_4 NPs. (a) HL-1 cells stained with fluo-4 calcium stain incubated with 2.0 μg/cm^2 hg-C_3N_4 NPs (+P) and photostimulation (+L) at 0 min, 10 min, and 30 min. Red circles indicate ROIs for $\Delta F/F_0$ plots. **(b)** $\Delta F/F_0$ plots of 8 different ROIs showing beating frequency of photostimulated HL-1 cells. **(c)** Isochromal maps of Hl-1 cells incubated with or without hg-

C_3N_4 NPs (+P; -P) and with or without photostimulation (+L; -L). Light source was 10 mW/cm^2 of 450 nm with pulse width of 100 ms and 1 Hz frequency. Scale bars are 275 µm.

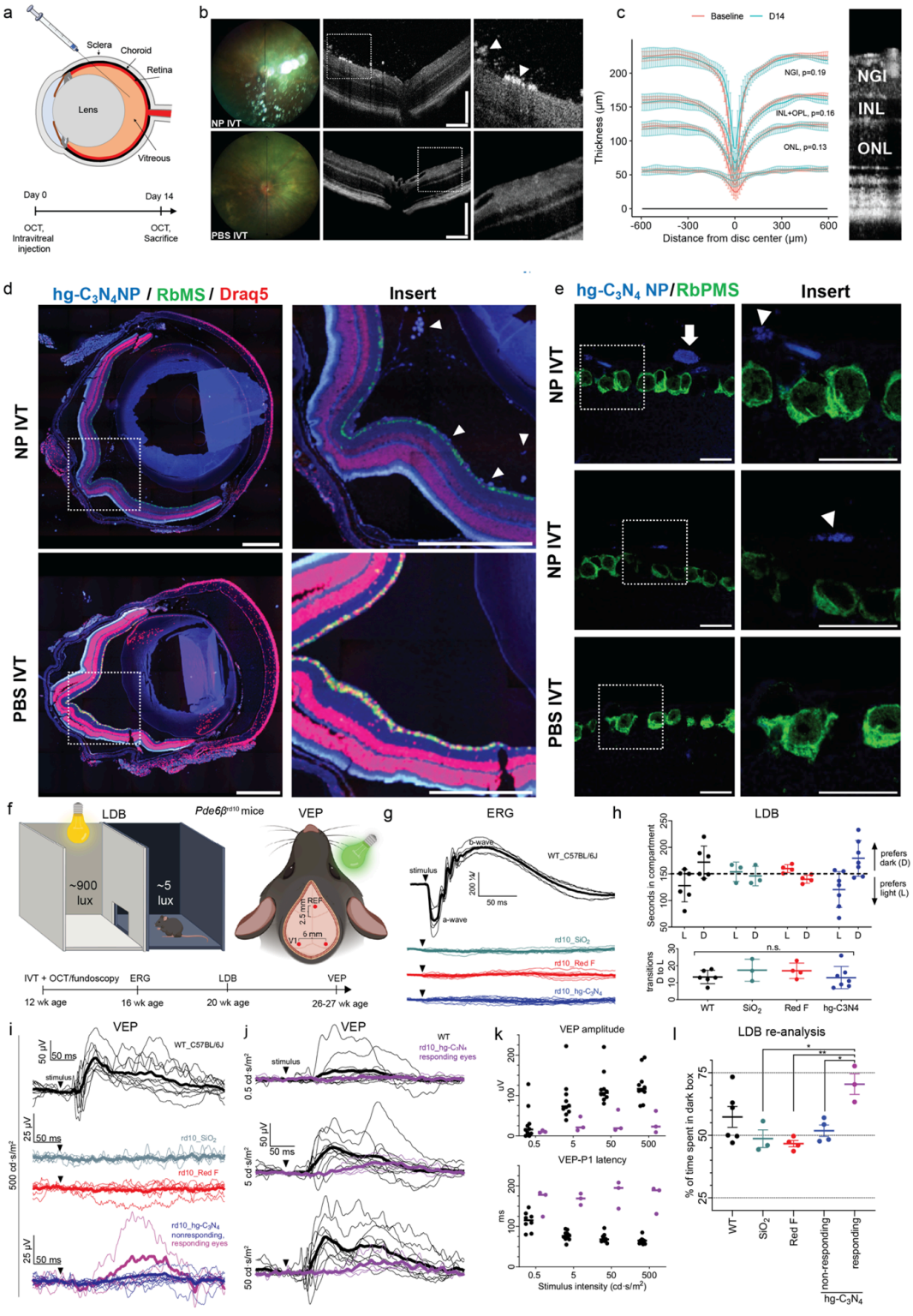

Figure 7

Intravitreal delivery of hg-C_3N_4 NPs is safe, results in NP adherence to the retinal surface near the RGCs and their axons, and restores light sensitivity in rd10 retinitis pigmentosa mice. (a) Schematic

drawing of the intravitreal injection procedure and experimental timeline. **(b)** Representative fundus images and optical coherence tomography scans from eyes intravitreally injected with hg-C_3N_4 NPs (NP IVT) or buffer (PBS IVT). The integrity of retinal layers is preserved and hyperreflective spots corresponding to aggregated NPs (white arrowheads) can be observed in the vitreous and on the retinal surface. Scale bars are 200 µm. **(c)** Position of retinal borders in the NP IVT eyes at baseline and D14 (mean ± sd) with comparisons of the mean thickness of interposed retinal layers. Paired t-test between mean thickness of specified retinal layers, baseline vs. D14. n = 6. NGI = combined thickness of retinal nerve fiber layer, ganglion cell layer and inner plexiform layer; INL = inner nuclear layer; OPL = outer plexiform layer; ONL = outer nuclear layer. **(d)** 20x widefield fluorescent images from the mice shown in (b) labeled with the RGC marker anti-RbPMS (green) and counterstained with Draq5 (red). The blue fluorescent NPs (white arrowheads) are attached to vitreous strands and the retinal surface. Scale bars are 500 µm. **(e)** Corresponding 63x confocal microscopy images. NPs (white arrowheads) are seen on the inner retinal surface near the RGCs. In some areas, NPs were engulfed by rounded cells, presumably hyalocytes (white arrow). Scale bars are 20 µm. (**f**) Scheme of visual function experiments in rd10 and WT mice. (**g**) Scotopic electroretinogram (ERG) waveforms (30 cd·s/m^2 flash). (**h**) Analysis of behavior in the light-dark box (LDB) test. (**i**) Visual evoked potentials (VEPs). Thick lines represent group-mean VEP waveforms whereas the thin lines represent responses from individual eyes (WT, n=10 eyes, N=6 mice; rd10_SiO^2, n=6 eyes, N=3 mice; rd10_Red F, n=8 eyes, N=4 mice; rd10_hg-C_3N_4, n=14 eyes, N=7 mice). (**j**) VEP waveforms in WT mice and responding individuals (n=3) from the hg-C_3N_4-injected rd10 mouse group across different stimulus intensities. (**k**) VEP amplitudes and latencies in responding eyes/hemispheres. (**l**) Analysis of dark preference in the LDB test after re-grouping the hg-C_3N_4-injected rd10 mice based on intervention successfulness. Statistical analysis was performed with one-way ANOVA and Tukey's test for multiple comparisons: *p<0.05, **p<0.01.

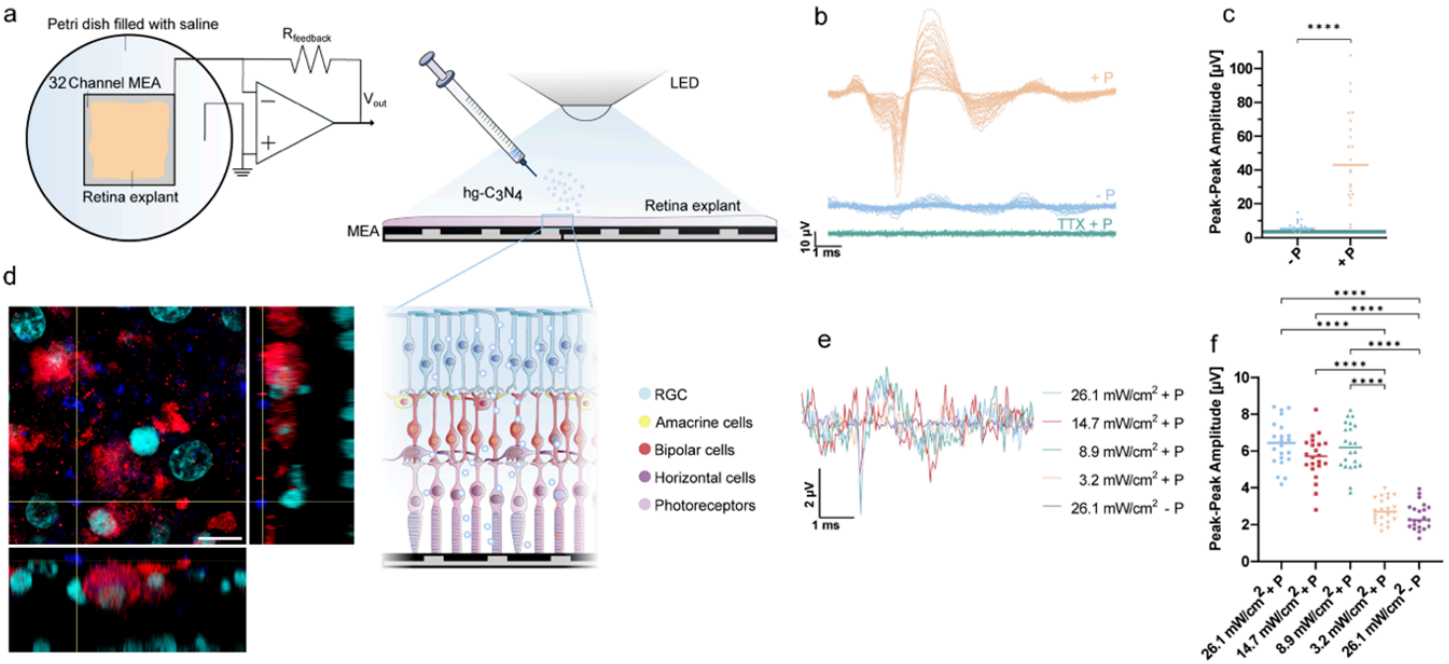

Figure 8

MEA recordings of porcine retina. (a) Scheme of the MEA retina measurement setup. Inset shows cellular structure of retinal tissue with RGC interacting with hg-C_3N_4 NPs. **(b)** Tracings of light-evoked potentials with 32 channel MEA while applying 1 ms 450 nm LED pulse, with 30 mW/cm^2. **(c)** Quantification of peak-peak amplitudes recorded for each channel of the 32 channel MEA. Turquoise horizontal line indicates 25% and 75% percentile of TTX silenced firing. Statistical analysis was perfomed using the unpaired two-tailed t-test where p<0.0001 is denoted as ****. **(d)** Fluorescent image of porcine retinal flat mounts obtained from tissue following settlement of hg-C_3N_4 NPs on the retinal ganglion cell layer. Scale bar is 10 µm. Blue is hg-C_3N_4, turquoise is Draq5, red is RbPMS **(e)** Average tracings of light-evoked potentials of 32 channels for different light doses of 100 ms 450 nm LED pulse. **(f)** Quantification of peak-peak amplitudes of light dose-response recordings. Statistical analysis was performed with one-way ANOVA and Tukey's test for multiple comparisons where p<0.0001 is denoted as **** .

Supplementary Files

This is a list of supplementary files associated with this preprint. Click to download.

- SupplementaryNaturecomm2024.docx
- VideoS1Internalization.avi
- VideoS2nonparticlecontrolplayedindoublespeed.avi
- VideoS33T3.mp4
- VideoS43T3dFF0.avi
- VideoS5HELA.mp4
- VideoS6HELAdFF0.avi
- VideoS7CMtoCM.mp4
- VideoS8CFtoCF.mp4
- VideoS9CFtoCM.mp4
- VideoS10with0minstimulation.avi
- VideoS11with10minstimulation.avi
- VideoS12with30minstimulation.avi